Current Biology 22, 269–277, February 21, 2012 ©2012 Elsevier Ltd All rights reserved DOI 10.1016/j.cub.2012.01.011

Article

Functional Biases in Visual Cortex Neurons with Identified Projections to Higher Cortical Targets

Beata Jarosiewicz,[1,5,*] James Schummers,[1,6] Wasim Q. Malik,[2,4] Emery N. Brown,[2,3,4] and Mriganka Sur[1,2,*]
[1]Picower Institute for Learning and Memory
[2]Department of Brain and Cognitive Sciences
[3]Division of Health Sciences and Technology
Massachusetts Institute of Technology, Cambridge, MA 02139, USA
[4]Department of Anesthesia, Critical Care and Pain Medicine, Massachusetts General Hospital, Harvard Medical School, Boston, MA 02114, USA

Summary

Background: Visual perception involves information flow from lower- to higher-order cortical areas, which are known to process different kinds of information. How does this functional specialization arise? As a step toward addressing this question, we combined fluorescent retrograde tracing with in vivo two-photon calcium imaging to simultaneously compare the tuning properties of neighboring neurons in areas 17 and 18 of ferret visual cortex that have different higher cortical projection targets.
Results: Neurons projecting to the posterior suprasylvian sulcus (PSS) were more direction selective and preferred shorter stimuli, higher spatial frequencies, and higher temporal frequencies than neurons projecting to area 21, anticipating key differences between the functional properties of the target areas themselves. These differences could not be explained by a correspondence between anatomical and functional clustering within early visual cortex, and the largest differences were in properties generated within early visual cortex (direction selectivity and length preference) rather than in properties present in its retinogeniculate inputs.
Conclusions: These projection cell groups, and hence the higher-order visual areas to which they project, likely obtain their functional properties not from biased retinogeniculate inputs but from highly specific circuitry within the cortex.

Introduction

Modular functional organization is a fundamental principle of cortical processing [1]. In primates, more than 30 specialized visual cortical regions are recognized, and they are organized into a loose hierarchy of ascending receptive field size and complexity [2–4]. In other species, such as carnivores, a number of homologous cortical areas have been described, and similar organization principles appear to hold [5, 6]. At the first stage of visual cortical processing, it is thought that functional specialization such as orientation selectivity arises through a combination of biased inputs arriving from thalamus [7] and elaboration and refinement of these biases by intracortical connectivity [8, 9].

Whether similar principles underlie the generation of functional specialization in higher cortical areas remains unknown. As a step toward addressing this issue, we have developed a method to test whether functional biases exist in the response properties of neurons in a lower-order cortical area that project differentially to either of two higher-order cortical areas downstream. By combining dual retrograde fluorescent labeling, which allows cells with distinct projection targets to be visualized in distinct colors, with in vivo two-photon calcium imaging, which makes it possible to characterize the tuning properties of those retrogradely labeled cells, we were able to directly compare the tuning properties of these two sets of projection neurons in primary visual cortex simultaneously and at single-cell resolution.

Of several high-order visual cortical areas that have been described in carnivores, we focused on two areas that receive direct projections from primary visual cortex and are at similar, intermediate stages of the visual processing hierarchy in the ferret, posterior suprasylvian sulcus (PSS) and area 21. PSS of ferrets is homologous to the posteromedial lateral suprasylvian area (PMLS) of cats [10–12] and is therefore a likely analog of monkey medial temporal cortex (MT) [5, 6, 13]; cells in PSS and PMLS are highly direction selective, show strong end suppression (i.e., the extension of stimuli outside of their receptive field centers inhibits their activity), and prefer high temporal frequencies [14–16]. Area 21 of ferrets is homologous to area 21a of cats [15, 17–19] and is therefore a likely analog of monkey V4 [6]; cells here are less direction selective, show length summation rather than length suppression (i.e., their responses increase monotonically with bar length), and prefer lower temporal frequencies [16, 20, 21]. We found that these differences in receptive field characteristics in PSS and area 21 are foreshadowed by biases in the tuning properties of spatially interleaved visual cortical neurons that project differentially to these two areas, supporting the hypothesis that the principles underlying the generation of functional specialization in higher-order cortical areas are similar to those that have been proposed for lower-order areas.

Results

To identify those neurons in early visual cortex that project to PSS versus to area 21, we injected a retrograde tracer (cholera toxin B, or CTB) conjugated to one of two different fluorescent markers (Alexa Fluor 555 or 594), one into area PSS and the other into area 21 of ferret visual cortex (see Experimental Procedures; see also Supplemental Experimental Procedures and Figure S1 available online). Injections were made at matched cortical locations representing similar, central locations of the visual field [19]. After neurons were retrogradely filled (5–12 days after the injection; see Table S1), we implanted a cranial window over posterior visual cortex, bulk loaded a region of either area 17 or area 18 containing both sets of retrogradely filled cells with the calcium indicator dye Oregon green 488-BAPTA, and characterized their activity in response to visual stimuli using in vivo two-photon imaging (Figure 1).

As expected from the anatomy of feedforward projections in cat visual cortex [22, 23], most of the retrogradely labeled cells

[5]Present address: Department of Neuroscience, Brown University, Providence, RI 02912, USA
[6]Present address: Max Planck Florida Institute, Jupiter, FL 33468, USA
*Correspondence: jarosiew@gmail.com (B.J.), msur@mit.edu (M.S.)

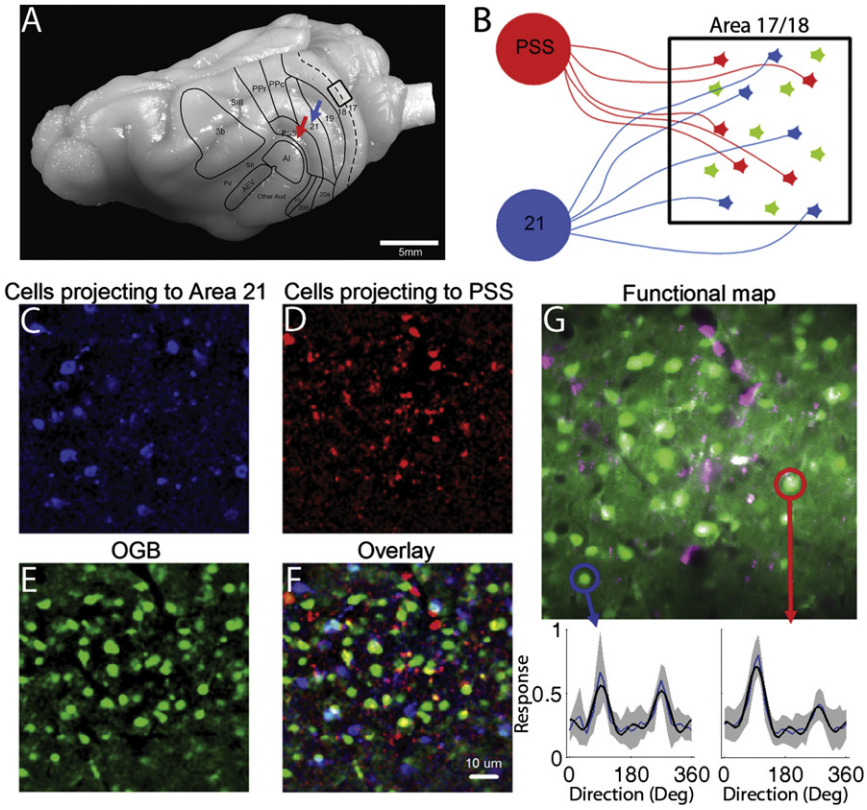

Figure 1. Labeling and Imaging Area 17/18 Cells that Project to Distinct Cortical Targets

(A) Location of visual areas in the ferret cortex (modified with permission from [51]). Injections of retrograde tracers CTB-594 and CTB-555 were made into PSS (red arrow) and area 21 (blue arrow) to label projection neurons in areas 17 and 18.

(B) Distinct sets of projection neurons in area 17/18 projecting to area 21 (blue) or PSS (red) could then be identified and bulk loaded with the calcium indicator dye Oregon green 488-BAPTA (OGB), allowing their physiological response features to be characterized.

(C–F) Example of an imaging region in area 17 (from ferret 8847) containing both projection cell types, bulk loaded with OGB.

(G) Calcium responses of individual neurons were obtained using two-photon imaging while parameterized visual stimuli were presented to the animal. Two channels, one configured for visualizing OGB and one for visualizing CTB-594, were imaged simultaneously during stimulus presentation. A "functional map" was created by collapsing these two-channel images across time. For data analysis, the average time series of the OGB fluorescence within each cell, bandpass filtered to reduce slow drift and high-frequency noise, was used to obtain the cell's tuning function. Two examples of direction tuning curves are shown, one from an area 21-projecting cell (circled in blue) and one from a PSS-projecting cell (circled in red) that were imaged in the same region in response to the same stimuli. The blue trace is the mean and the gray cloud is the standard error of the response to each direction (with the preferred direction centered at 90°); the black trace is the tuning curve fitted with a harmonic model.

See also Supplemental Experimental Procedures and Figure S1.

in areas 17 and 18 were found in layers 2/3, whose depth from the cortical surface (~120–300 μm) was accessible with two-photon calcium imaging. Importantly, in most animals, it was possible to locate one or more 250 × 250 μm imaging regions containing cells projecting to each area, which allowed for within-animal comparisons between projection cell types and controlled for other factors that might affect neural responses, such as eccentricity and depth of anesthesia.

In each animal, we assigned each imaging site to either area 17 or 18 (see Figure 1A) based on its distance from the posterior pole of cortex, its overall spatial frequency preference, and its retinotopy [24, 25] (see Figure S1 and Table S1). Taken as a whole, spatial and temporal frequency preferences tended to be lower, and direction selectivity tended to be higher, in area 18 than area 17 (see Figures S2–S5). However, the differences that we observed between projection cell types were consistent within each imaging site, irrespective of its location (see Figures 2, 3, 4, and 5); thus, data from areas 17 and 18 are grouped together for statistical power in the analyses comparing the tuning preferences of cells projecting to PSS versus those of cells projecting to area 21 (comparisons are also shown separately for imaging sites in area 17 versus area 18 in the Supplemental Information). Below, when the two areas are grouped together, we refer to them as "area 17/18" [26].

Direction and Orientation Selectivity

Direction and orientation selectivity were characterized by presenting gratings whose drift direction abruptly changed by 10° each second. PSS-projecting and area 21-projecting cells were identified, and a harmonic regression model was fit to their responses to this periodic stimulus (see Supplemental Experimental Procedures and Figures S1G and S1H). Cells projecting to PSS were significantly more direction selective than cells projecting to area 21 (Figures 2A–2C), whether the cells were located in area 17 or area 18 (Figures S2A, S2B, S2D, and S2E). Calculating the direction selectivity index (DSI) of each cell using the vector average of responses in all directions, the mean and standard error of the mean of the DSI of PSS-projecting area 17/18 cells (138 cells from 13 imaging sites in 11 ferrets) was 0.25 ± 0.01, and that of area 21-projecting area 17/18 cells (113 cells from 10 imaging sites in 9 ferrets) was 0.17 ± 0.01 (t test, $p < 10^{-8}$, treating cells from all imaging sessions as independent samples). This difference was confirmed using another common method of assessing direction selectivity, by comparing the peak responses in the preferred versus nonpreferred direction: $DSI_p = (P - N)/(P + N)$, where P is the response in the preferred direction and N is the response in the nonpreferred direction. The mean DSI_p of PSS-projecting cells was 0.28 ± 0.02, and that of area 21-projecting cells was 0.16 ± 0.01 (t test, $p < 10^{-9}$). These results support the results of an electrophysiology study in macaques showing that MT-projecting cells are more strongly direction selective than the average V1 cell [27]; we extend these results to a new species using a different technique, and we directly and simultaneously compare two homologous cell types that are known to be spatially intermingled within early visual cortex but that differ in their projection targets.

The location of the injection sites and imaging chamber was consistent across animals, so that the imaged cells in areas 17

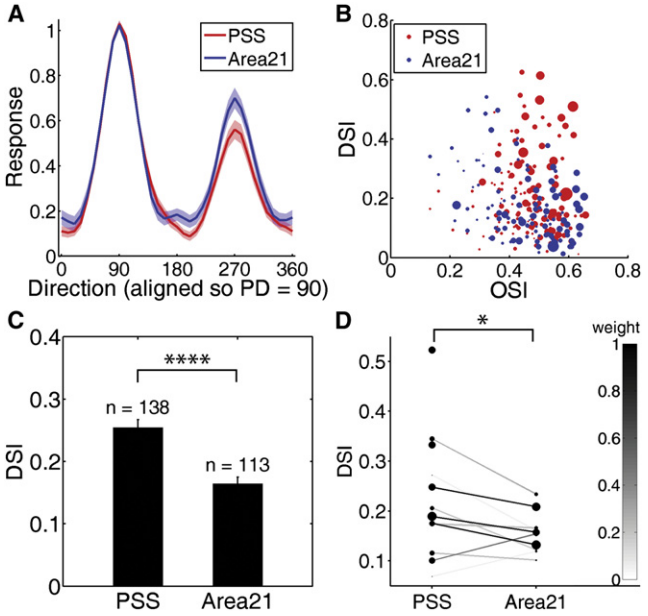

Figure 2. Direction and Orientation Selectivity

Area 17/18 cells projecting to PSS are more direction selective than area 17/18 cells projecting to area 21, but the cell groups do not differ in orientation selectivity.

(A) Weighted mean of all direction tuning curves (each cell's curve was scaled from 0 to 1 and its preferred direction was aligned at 90° before averaging). The colored shading indicates the pointwise 95% confidence interval (CI) of the weighted mean.

(B) Each cell's direction selectivity index (DSI) is plotted against its orientation selectivity index (OSI), each obtained using vector averaging (see Experimental Procedures). The size of each dot is proportional to the signal-to-noise ratio (SNR) of that cell's harmonic fit, which was used to weight the cell in the statistical analyses.

(C) Weighted mean and standard error of the weighted mean (SEM) of the DSI of each cell group. Treating all cells as independent samples, PSS-projecting cells were significantly more direction selective than area 21-projecting cells ($p < 10^{-8}$). Orientation selectivity did not differ between the two cell groups.

(D) Within-site analysis of DSI. Each "barbell" represents one imaging site; the dots without bars come from sites in which only one cell type was imaged. The size of each dot reflects the total weight contributed by that cell group in that imaging site (i.e., the number of cells × the mean weight of the cells). The darkness of each line indicates the total weight from both cell groups, which was used to weight that imaging site in a paired within-site t test (see Experimental Procedures). PSS-projecting cells were significantly more direction selective than their neighboring area 21-projecting cells ($p < 0.05$).

+0.05 < p < 0.10; *p < 0.05; **p < 0.01; ***p < 0.001; ****p < 0.001. See also Figure S2.

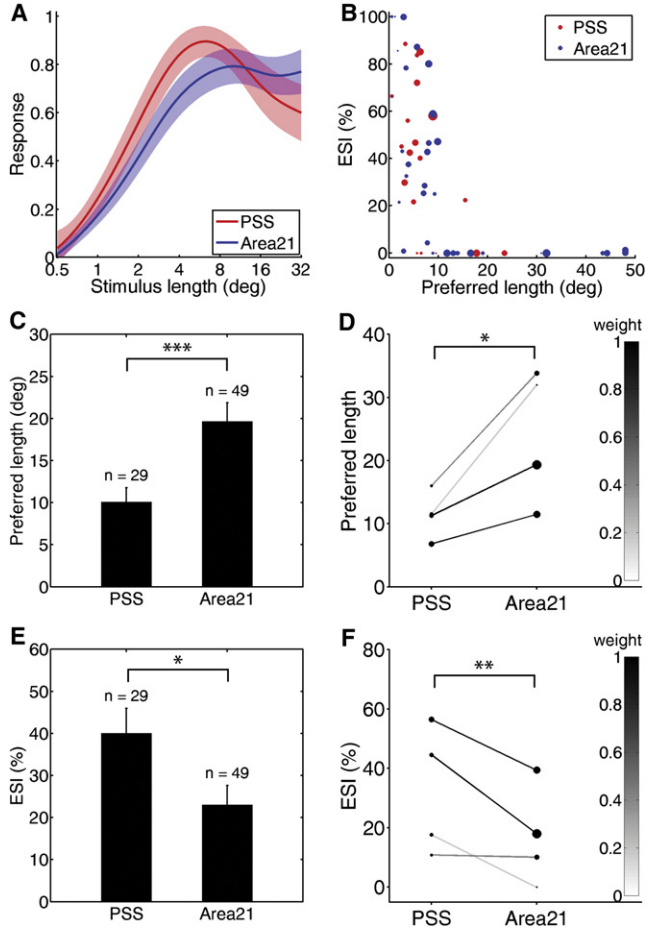

Figure 3. Length Tuning

Area 17/18 cells projecting to area 21 prefer longer stimuli than area 17/18 cells projecting to PSS.

(A) Pointwise weighted mean and 95% CI of all fitted length tuning curves.

(B) Each dot represents one cell's preferred length plotted against its end-suppression index (ESI, defined as the response to the preferred length minus the response to the longest length, as a percentage of the response to the preferred length). The size of the dot is proportional to the weight of that cell.

(C) Weighted mean and SEM of the preferred length of each cell group, treating all cells across all imaging sites as independent samples. Area 21-projecting cells had higher preferred lengths than PSS-projecting cells ($p < 0.001$).

(D) Within-site analysis of preferred length (see Figure 2 legend). Despite variability in length preferences across imaging sites, area 21-projecting cells had significantly higher preferred lengths than their neighboring PSS-projecting cells from the same imaging site ($p < 0.05$).

(E) Weighted mean and SEM of the ESI, treating all cells as independent samples. The responses of PSS-projecting cells were more strongly suppressed by long stimuli than area 21-projecting cells ($p < 0.05$).

(F) Within-site analysis of ESI, showing that this difference is also significant when comparing neighboring area 21-projecting and PSS-projecting cells ($p < 0.01$).

+0.05 < p < 0.10; *p < 0.05; **p < 0.01; ***p < 0.001; ****p < 0.001. See also Figure S3.

and 18 had similarly located receptive field eccentricity (approximately 0° to 15° azimuth and 0° to −15° elevation; see Figure S1A). Nevertheless, because tuning preferences are known to vary across the surface of areas 17 and 18 in ferrets [25] and the number of cells in one cell group was not necessarily the same as the number of cells in the other cell group at a given imaging site, it was important to control for variability in tuning properties across animals and across imaging sites. Thus, we also tested whether the observed differences between projection cell types also exist within individual imaging sites. For each imaging site in which at least one cell of each type was imaged (Figure 2D), we computed the mean DSI of the PSS-projecting cells and the mean DSI of the area 21-projecting cells and used these two DSIs as one set of data points in a paired t test. Across the ten imaging sites in which both cell types were imaged, PSS-projecting cells had a significantly higher DSI than their neighboring area 21-projecting cells ($p < 0.05$). Thus, PSS-projecting cells were more direction selective than area 21-projecting cells, even when these neurons were spatially intermingled within the same 250 × 250 μm imaging region.

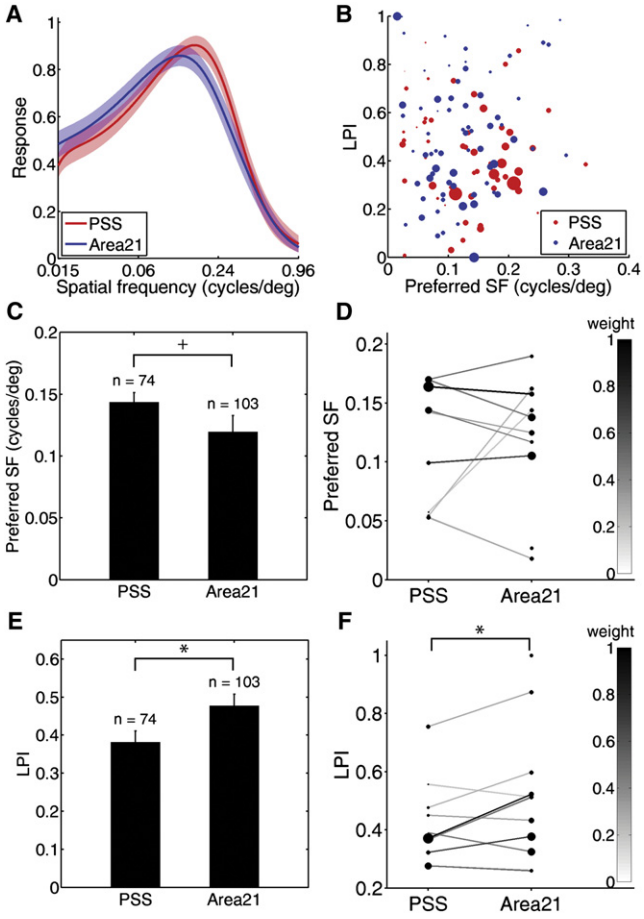

Figure 4. Spatial Frequency Tuning

Area 17/18 cells projecting to area 21 respond more strongly at low spatial frequencies (SF) than area 17/18 cells projecting to PSS.

(A) Weighted mean and 95% CI of all fitted SF tuning curves.

(B) Each dot represents one cell's preferred SF plotted against its low-pass index (LPI). The size of the dot is proportional to the weight of that cell.

(C) Weighted mean and SEM of the preferred SF of each cell group, treating all cells as independent samples. PSS-projecting cells showed a trend toward having higher preferred SF than area 21-projecting cells, though this trend did not reach significance ($p = 0.057$).

(D) Within-site analysis of preferred SF did not reveal a significant difference between cell groups imaged from the same site.

(E) Weighted mean and SEM of the LPI, treating all cells as independent samples. Area 21-projecting cells were significantly more low pass than PSS-projecting cells ($p < 0.05$).

(F) Within-site analysis of LPI. Area 21-projecting cells were significantly more low pass than their neighboring PSS-projecting cells ($p < 0.05$).

+0.05 < p < 0.10; *p < 0.05; **p < 0.01; ***p < 0.001; ****p < 0.001. See also Figure S4.

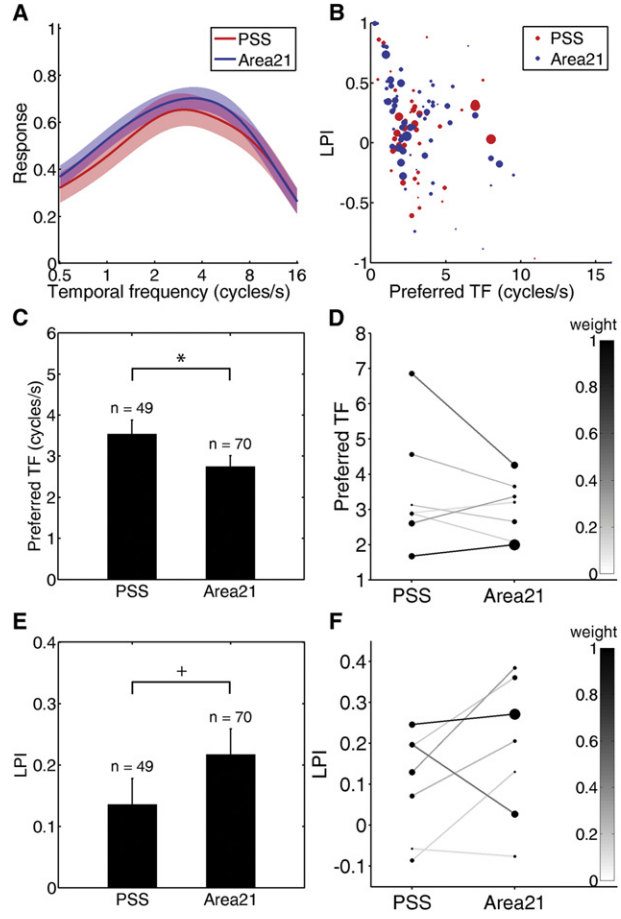

Figure 5. Temporal Frequency Tuning

Area 17/18 cells projecting to PSS prefer higher temporal frequencies (TF) than area 17/18 cells projecting to area 21.

(A) Weighted mean and 95% CI of all fitted TF tuning curves.

(B) Each dot represents one cell's preferred TF plotted against its LPI. The size of the dot is proportional to the weight of that cell.

(C) Weighted mean and SEM of the preferred TF of each cell group, treating all cells as independent samples. PSS-projecting cells preferred higher TFs than area 21-projecting cells ($p < 0.05$).

(D) Within-site analysis of preferred TF did not reveal a significant difference between cell groups imaged from the same site.

(E) Weighted mean and SEM of the LPI, treating all cells as independent samples. Area 21-projecting cells tended to be more low pass than PSS-projecting cells, though this difference did not reach significance ($p = 0.086$).

(F) Within-site analysis of LPI also did not reveal a significant difference between cell groups imaged from the same site.

+0.05 < p < 0.10; *p < 0.05; **p < 0.01; ***p < 0.001; ****p < 0.001. See also Figure S5.

PSS-projecting and area 21-projecting area 17/18 cells did not differ in their orientation selectivity (Figures 2A and 2B). The mean of the orientation selectivity index (OSI) of PSS-projecting cells was 0.50 ± 0.01, and the mean OSI of area 21-projecting cells was 0.49 ± 0.01, as measured using the vector average of responses in the 180° centered around the preferred direction. This was confirmed using another common method of assessing orientation selectivity, the half-width at half-height of the orientation tuning curve: the mean half-width at half-height for PSS-projecting cells was 36.5° ± 0.5°, and the mean for area 21-projecting cells was 35.3° ± 0.7°. These differences were also not significant.

Length Tuning

Length tuning was characterized by presenting one cycle of a grating at the optimal orientation for the imaging region and varying its length using an episodic paradigm (see Supplemental Experimental Procedures and Figures S1I and S3K). The integral of a difference of Gaussians was fit to each cell's response to the different lengths [28, 29]. The preferred length (the length at the peak of the fitted curve) and end-suppression index (ESI, the percent by which the response to the longest length is suppressed relative to the preferred length) were then obtained for each cell and compared across cell groups.

Area 17 cells projecting to area 21 preferred longer stimuli than area 17 cells projecting to PSS (Figures S3A and S3B), as

did area 18 cells (Figures S3F and S3G), and when cells in area 17 and 18 were grouped together (Figure 3), the differences in length preference between the two projection cell types were strongly statistically significant. The mean of the preferred length of area 21-projecting area 17/18 cells (29 cells from 4 imaging sites in 4 ferrets) was 19.7° ± 2.2°, and that of PSS-projecting area 17/18 cells (49 cells from the same 4 imaging sites in 4 ferrets) was 10.1° ± 1.7° (t test, $p < 0.001$, treating cells from all imaging sessions as independent samples). Additionally, the mean ESI of the area 21-projecting cells (23.0% ± 4.6%) was significantly lower than that of PSS-projecting cells (40.1% ± 5.9%; t test, $p < 0.05$). These differences in length preferences were also consistent within individual imaging sessions (Figures 3D and 3F; within-site paired t test, preferred length: $p < 0.01$; ESI: $p < 0.001$). Thus, even among area 17/18 neurons that are spatially intermingled within the same 250 × 250 μm imaging region, there are clear differences in the degree of length summation and end suppression of individual neurons that project to PSS versus to area 21.

Spatial Frequency Tuning

Spatial frequency (SF) tuning was characterized by presenting a grating at the optimal orientation and temporal frequency for the imaging region and varying its SF using an episodic paradigm (see Figures S1I and S4K). Each cell's SF tuning curve was fit to a difference of Gaussians centered at 0, representing the power spectrum of the center and surround of the receptive field [30]. The preferred SF (the SF at the peak of the fitted curve) and a low-pass index (LPI, the difference in the response to low versus high SF, normalized by the peak height) were then obtained for each cell and compared across cell groups.

Area 17/18 cells projecting to PSS had different SF preferences than area 17/18 cells projecting to area 21 (Figures 4 and S4A–S4J), though these differences were smaller than the differences in direction selectivity and length tuning. The mean of the preferred SF of PSS-projecting area 17/18 cells (74 cells from 9 imaging sites in 8 ferrets) was 0.144 ± 0.008 cycles/°, and that of area 21-projecting area 17/18 cells (103 cells from 10 imaging sites in 9 ferrets) was 0.120 ± 0.013 cycles/°. This difference in peak SF preference did not reach significance when treating all cells from all imaging sessions as independent samples, or within imaging sessions (t test, $p = 0.057$; Figure 4D). However, the area 21-projecting area 17/18 cells were slightly but significantly more low pass (LPI = 0.477 ± 0.030) than the PSS-projecting cells (0.381 ± 0.029; $p < 0.05$) when treating all cells as independent samples (Figure 4E) and within individual imaging sessions (Figure 4F; within-site paired t test, $p < 0.05$).

Temporal Frequency Tuning

Temporal frequency (TF) tuning was characterized by presenting a grating at the optimal orientation and SF for the imaging region and varying its TF using an episodic paradigm (see Figures S1I and S5K). The responses were fit to the same tuning curve model used for SF, a difference of Gaussians centered at zero, and the preferred TF and LPI were compared across cell groups.

Area 17/18 cells projecting to PSS preferred higher TFs than area 17/18 cells projecting to area 21 (Figures 5 and S5A–S5J), though these differences were also less robust than the differences in direction selectivity and length preference. The mean preferred TF of PSS-projecting area 17/18 cells (49 cells from 7 imaging sites in 6 ferrets) was 3.54 ± 0.33 cycles/s, and that of area 21-projecting area 17/18 cells (70 cells from the same imaging sites) was 2.75 ± 0.26 cycles/s (t test, $p < 0.05$, treating all cells from all imaging sessions as independent samples). The mean LPI of the PSS-projecting cells (0.136 ± 0.042) and area 21-projecting cells (0.217 ± 0.042) showed a trend in the same direction (area 21-projecting cells preferring lower TFs), but this difference did not reach significance ($p = 0.086$). The within-site differences also did not reach significance (Figures 5D and 5F).

Anatomical and Functional Clustering

To test whether the observed relationship between functional properties and anatomical projection target could be explained by overlapping patterns of functional and anatomical clustering in area 17/18, we measured for each imaging site the degree of anatomical and functional clustering and tested for a correspondence between the two (Figure 6). To test for anatomical clustering (Figures 6A–6C), same-group and different-group anatomical clustering ratios (ACRs) were compared for each imaging site containing at least two cells in each projection target group. Of the nine such imaging sites in which DSI was measured, the same-group ACRs were significantly higher than the different-group ACRs in three imaging sites (see Figure S2G for each site's p values), indicating that cells with the same projection target tended to be nearer to each other than cells with different projection targets in those three imaging sites. The imaging sites in which length, SF, and TF preference were assessed contained many of the same cells as one another and as the DSI sites, because multiple functional features were measured for each imaging site; however, the locations of the cell centers might have shifted and cells might have appeared or disappeared over time due to drift in the depth of the focal plane, so ACRs were also measured for these sites to allow for a comparison between functional and anatomical clustering within each imaging site. Of the 19 functional measure/imaging site combinations, 6 were significantly anatomically clustered (Figure S6).

To test for functional clustering in each imaging site (Figure 6D), the absolute difference in the tuning for the measured parameter in that imaging site was computed for each nearest-neighbor cell pair, and its p value was obtained by comparing the mean difference to a bootstrapped null distribution. For imaging sites in which DSI was measured, the weighted mean DSI difference among nearest neighbors was significantly lower than expected by chance in 4 of the 13 imaging sites (Figure S2G), indicating that cells nearer to each other in those imaging sites tended to have similar direction selectivity. None of the 6 imaging sites in which length preference was measured had significant functional clustering for preferred length, 4 of the 10 imaging sites in which SF was measured had significant functional clustering for preferred SF, and 1 of the 8 imaging sites in which TF was measured had significant functional clustering for preferred TF (Figure S6).

In the two imaging site/functional parameter combinations that were significant for both anatomical and functional clustering (Figures 6A and 6B), we tested for a significant correspondence between functional and anatomical clustering by comparing same-group to different-group nearest-neighbor functional differences (Figure 6E). The nearest-neighbor functional differences between cell pairs from the same anatomical group were not significantly different from the nearest-neighbor functional differences between cell pairs from different

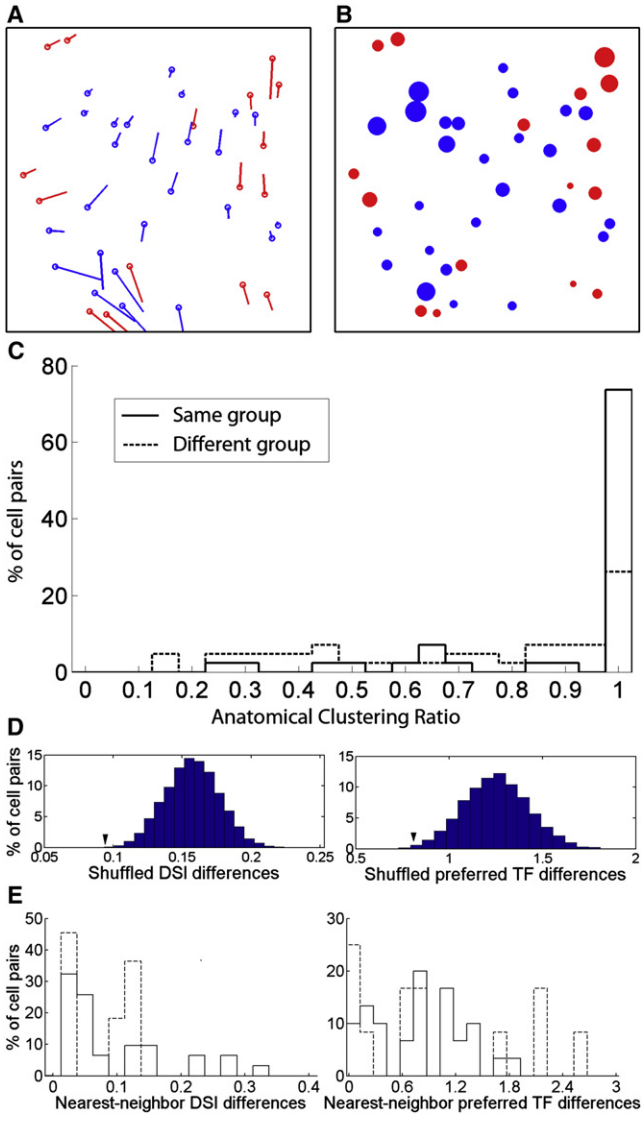

Figure 6. Functional and Anatomical Clustering

(A and B) A direction selectivity map (A) and a temporal frequency preference map (B) are shown for imaging site 8545(2), which was the only imaging site significant for both anatomical clustering and functional clustering for any functional feature. (See Figures S2G and S6 for maps of all imaging sites and all features.) The center of each cell's location in the imaging site is marked by a circle (red indicates cells projecting to PSS; blue indicates cells projecting to area 21.)

(A) Each cell's preferred motion direction is indicated by a line extending from the circle, and its relative DSI is represented by the length of the line (longer lines represent higher direction selectivity).

(B) Each cell's relative temporal frequency preference is represented by the size of the dot (larger dots represent higher preferred temporal frequency).

(C) Anatomical clustering ratio (ACR) for all nearest-neighbor cell pairs with the same (solid line) versus opposite (dashed line) projection target in this imaging site. The same-group ACRs were significantly higher than the different-group ACRs (sign test, n = 42 cells; sign = 85; Z = 3.24; $p < 0.005$), indicating that cells with the same projection target tended to be nearer to each other than cells with different projection targets.

(D) Functional clustering results. Each histogram shows the actual weighted mean of the nearest-neighbor functional differences (black arrowhead) relative to a null distribution generated by randomly shuffling the DSIs (left) or preferred TFs (right) across cells. The weighted mean DSI difference among nearest neighbors (left) was significantly lower than expected by chance ($p < 0.001$), indicating significant functional clustering in this imaging site for direction selectivity. The weighted mean TF preference among nearest neighbors (right) was also significantly lower than expected by chance ($p < 0.01$), indicating significant functional clustering for TF preference.

(E) Although this imaging site was significantly clustered both anatomically and functionally, there was no significant correspondence between its functional and anatomical clustering: the nearest-neighbor functional differences between cell pairs from the same anatomical group (solid line) were not significantly different from the nearest-neighbor functional differences between cell pairs from different anatomical groups (dashed line) (left: DSI, weighted t test, p = 0.79; right: TF, weighted t test, p = 0.65).

anatomical groups (DSI: weighted t test, p = 0.79; TF: weighted t test, p = 0.65); thus, although anatomical and functional clustering were both observed independently, there was no evidence for a correspondence between them in any imaging site.

Discussion

These results demonstrate that two populations of projection neurons that are spatially intermingled within early visual cortex have different sets of response properties that relate to the function of their respective projection targets. A previous elegant but difficult study had reported that V1 cells in macaques projecting to MT were more direction selective than the average V1 neuron by combining single-cell electrophysiological recording in V1 with antidromic stimulation in MT [27]. However, of the 745 neurons recorded in V1, only 12 were found to be antidromically activated from MT, and data were successfully collected from 9 of them. Our method provides a more powerful way to probe the relationship between anatomical connectivity and physiology simultaneously for large populations of individual neurons with known spatial relationships and multiple known projection targets.

In the present study, we found that PSS-projecting and area 21-projecting area 17/18 cells in ferrets exhibit differences in direction selectivity and stimulus length preferences, and to a lesser degree in temporal frequency preferences, that reflect the reported tuning properties of cells in their projection targets. It would be ideal to quantitatively compare the differences in tuning properties of these input cells to the tuning properties of their targets using the same methods; however, a direct comparison would be difficult because it would require recording the responses of identified pre- and postsynaptic partners. Furthermore, it is unlikely that the same stimuli could elicit robust responses in all three areas, given that tuning is known to evolve across steps in cortical processing, and in different ways along the dorsal and ventral pathways [2–4]. Although some properties of higher cortical areas are anticipated by area 17/18 responses, not all properties are equally anticipated: area 17/18 cells that project to PSS versus area 21 are most distinguished by direction selectivity, followed by length summation (or end stopping), spatial frequency selectivity, and temporal frequency selectivity. One property is seemingly anomalous: we find that PSS-projecting cells tend to prefer higher spatial frequencies than area 21-projecting cells, whereas cat PMLS cells are reported to have larger receptive fields than area 21a cells at matched receptive field eccentricity [15]. Our results therefore indicate that although biases exist in the tuning properties of cells in lower cortical areas depending on their higher-order projection targets, these input biases are further summed, amplified, and reshaped by target area circuitry [7, 8, 31].

Although we examined small (250 × 250 μm) regions of early visual cortex, we found no evidence for a correspondence between functional and anatomical clustering; i.e., in imaging regions that were significantly clustered both anatomically and functionally, neighboring cell pairs with the same projection targets did not have more similar tuning than neighboring cell pairs with different projection targets. In the absence of clustering correspondence, how might such precise, cell-specific functional-anatomical "sorting" arise?

It has been proposed that information channels originating in the retina maintain at least partial segregation through V1 into higher cortical processing streams [17, 32, 33]; however, mounting evidence argues against this possibility [34–36]. To the extent that PSS can be considered a part of the dorsal processing stream, and area 21 a part of the ventral processing stream, our findings provide further evidence against this hypothesis: the largest differences between PSS and area 21-projecting area 17/18 cells were in those functional properties that are thought to be cortically generated (direction selectivity and length preferences), not in the properties thought to be attributable to X versus Y channel inputs (spatial and temporal frequency preferences) [37, 38]. Furthermore, if we take the longer length preferences and tendency toward lower spatial frequency preferences of area 21-projecting cells as compared to PSS-projecting cells as evidence for larger receptive fields (or weaker surround inhibition), then these differences are in the opposite direction of those predicted by segregated X versus Y channel inputs.

Another possible source of the projection target-specific tuning biases in early visual cortical cells is spatially precise feedback from the higher-order areas to which they project. Indeed, well-specified functions in higher-order areas can contribute to the functional specialization of their inputs: training an artificial neural network to produce desired input-output transformations can create apparent "tuning" in the hidden layer [39, 40], and the tuning of randomly selected subsets of neurons in monkey motor cortex can be altered by changing the way their spiking activity is decoded downstream in a brain-computer interface [41]. Such feedforward-feedback interactions might play a crucial role in creating the functional biases present in the inputs to a cortical area.

The biases arising within early visual cortex might be elaborated in their target structures to generate stronger functional specialization by utilizing ubiquitous connectivity principles, similar to the way slight biases in orientation selectivity present in retinal and lateral geniculate nucleus cells [42, 43] are sharpened in V1 into strong orientation tuning by combining feedforward and recurrent inputs with the spike threshold [7–9]. Consistent with this proposal, we find that the direction selectivity of PSS-projecting area 17/18 cells is higher than area 21-projecting cells, and it is reported to be higher still within PSS [14]. Furthermore, there is evidence that biased inputs can contribute to the emergence of new computations across a single step of visual processing. For example, a large fraction of cells in monkey MT can resolve the aperture problem [44] and signal the global motion direction of a plaid pattern [45] despite the fact that V1 cells, even those projecting to MT, only signal the directions of its individual components [27, 45]; it has been proposed that global motion selectivity in MT can arise from component-selective V1 inputs if they are direction selective and end stopped [46, 47]. Here, we provide evidence supporting the mechanisms proposed in such models by showing that area 17/18 inputs to PSS (the ferret analog of MT) are indeed more direction selective and more end stopped than area 17/18 inputs to area 21 (the ferret analog of V4). The methods used here could be expanded to other sensory modalities and higher cortical areas to further support or constrain models of how new computations emerge across stages in cortical processing.

Experimental Procedures

Animals and Tracer Injection Surgery

Experiments were performed on 12 male ferrets 41–78 days old at the start of the experiment. All experimental procedures were approved by the MIT Institutional Animal Care and Use Committee and adhered to National Institutes of Health (NIH) guidelines. Pressure injections of tracer were made along the mediolateral extent of PSS (see Figure S1) and, in 10 of the 12 animals, along the mediolateral extent of area 21. PSS and area 21 were visually identified.

Two-Photon Imaging

Approximately 7 days after tracer injection, the functional properties of retrogradely labeled cells in area 17/18 were characterized using two-photon calcium imaging [48, 49]. A region in the cranial window was located that contained tracer-filled cells of both projection cell types, and two z stacks were taken from the cortical surface to 250–300 μm below the cortical surface, each with excitation and filter settings optimized for one of the tracers. Freshly prepared calcium indicator dye (Oregon green 488-BAPTA, OGB) was injected ~200 μm below the cortical surface at the chosen imaging site. Another set of z stacks was taken with an additional channel for imaging OGB, and an imaging depth was selected that contained a large number of traced cells. 256 × 256 pixel (~250 × 250 μm) images were captured from this plane at 1 Hz while visual stimuli were presented on an LCD monitor placed ~10 cm in front of the animal.

Direction and orientation selectivity

A "periodic" stimulus presentation paradigm was used for assessing direction and orientation selectivity: continuously drifting gratings were presented whose orientation and drift direction changed by 10° increments every second. Each trial consisted of three cycles around the circle, and trials were repeated 3–10 times during the course of an experiment. The drift-corrected, smoothed fluorescence time series for each cell were concatenated across trials and a tuning curve was obtained by fitting a harmonic regression model [50] (see Figures S1G and S1H). The direction selectivity index (DSI) was obtained from the fitted tuning curves using a vector average of the responses over the whole tuning curve, and separately by comparing the heights of the peaks in the preferred and nonpreferred direction (DSI_p). An orientation selectivity index (OSI) was computed using a vector average of the 180° of the direction tuning curve centered around the preferred direction, and separately as the half-width at half-height of the fitted curve.

Length, Spatial Frequency, and Temporal Frequency Tuning

An "episodic" stimulus presentation paradigm was used to assess length, spatial frequency (SF), and temporal frequency (TF) tuning. In each trial, stimulus "off" periods alternated with stimulus "on" periods in sets of four frames. In each "on" period, the parameter whose tuning function was being measured (length, SF, or TF) varied along a $\log_2$ scale while the rest of the parameters were held constant. Trials were repeated 6–10 times during the course of an experiment. Response amplitudes for each parameter value were obtained by fitting the filtered, baseline-corrected fluorescence signal with a sinusoid whose period matched the stimulus on/off cycle and whose amplitude reflected the cell's response to the stimulus (see Figure S1I), and tuning curves were obtained from these amplitudes by weighted least-squares regression to a difference of Gaussians (DoG) model for SF and TF tuning [30], or to the integral of a DoG model for length tuning [28] (see Figures S3–S5). The peaks of these tuning curves and a "low-pass index" characterizing their asymmetry around the peak were compared between cell groups.

Statistical Analysis

Instead of ignoring across-cell variability or simply discarding cells whose responsiveness to the parameter of interest did not exceed some arbitrary threshold, we weighted each cell in the statistics by its responsiveness to the parameter of interest (see Supplemental Experimental Procedures). Weighted t tests were used to compare response preferences across

groups, first treating all cells across all imaging sites as independent samples. Second, to control for factors that might affect neural responses, such as eccentricity of a given imaging site or the animal's depth of anesthesia, we also tested whether differences between cell groups existed within each imaging site: for each tuning parameter being compared, the weighted mean was obtained for each of the two cell groups in each imaging site that had at least one cell of each type. Each imaging site's pair of means was then used as one sample in a paired t test, weighting each imaging site by the total number of cells in that imaging site. Tests for anatomical and functional clustering are described in detail in Supplemental Experimental Procedures.

Supplemental Information

Supplemental Information includes six figures, one table, and Supplemental Experimental Procedures and can be found with this article online at doi:10.1016/j.cub.2012.01.011.

Acknowledgments

The authors would like to thank Amanda Mower, Beau Cronin, Ian Wickersham, Ethan Meyers, Paul Manger, Nicolas Masse, Hongbo Yu, Brandon Farley, Caroline Runyan, and Travis Emery for their contributions. This work was supported by Ruth L. Kirschstein National Research Service Award 5F32NS054390 (B.J.), NIH grants EY018648 and EY07023 (M.S.), and NIH grants DP1 OD003646 and EB006385 (E.N.B.).

Received: December 2, 2011
Revised: January 5, 2012
Accepted: January 5, 2012
Published online: February 2, 2012

References

1. Kaas, J.H. (1997). Topographic maps are fundamental to sensory processing. Brain Res. Bull. *44*, 107–112.
2. Felleman, D.J., and Van Essen, D.C. (1991). Distributed hierarchical processing in the primate cerebral cortex. Cereb. Cortex *1*, 1–47.
3. Goodale, M.A., and Milner, A.D. (1992). Separate visual pathways for perception and action. Trends Neurosci. *15*, 20–25.
4. Ungerleider, L.G., and Mishkin, M. (1982). Two cortical visual systems. In Analysis of Visual Behavior, D.J. Ingle, M.A. Goodale, and R.J.W. Mansfield, eds. (Cambridge, MA: MIT Press), pp. 549–586.
5. Lomber, S.G., Payne, B.R., Cornwell, P., and Long, K.D. (1996). Perceptual and cognitive visual functions of parietal and temporal cortices in the cat. Cereb. Cortex *6*, 673–695.
6. Payne, B.R. (1993). Evidence for visual cortical area homologs in cat and macaque monkey. Cereb. Cortex *3*, 1–25.
7. Ferster, D., and Miller, K.D. (2000). Neural mechanisms of orientation selectivity in the visual cortex. Annu. Rev. Neurosci. *23*, 441–471.
8. Somers, D.C., Nelson, S.B., and Sur, M. (1995). An emergent model of orientation selectivity in cat visual cortical simple cells. J. Neurosci. *15*, 5448–5465.
9. Sompolinsky, H., and Shapley, R. (1997). New perspectives on the mechanisms for orientation selectivity. Curr. Opin. Neurobiol. *7*, 514–522.
10. Cantone, G., Xiao, J., and Levitt, J.B. (2006). Retinotopic organization of ferret suprasylvian cortex. Vis. Neurosci. *23*, 61–77.
11. Homman-Ludiye, J., Manger, P.R., and Bourne, J.A. (2010). Immunohistochemical parcellation of the ferret (Mustela putorius) visual cortex reveals substantial homology with the cat (Felis catus). J. Comp. Neurol. *518*, 4439–4462.
12. Hupfeld, D., Distler, C., and Hoffmann, K.-P. (2007). Deficits of visual motion perception and optokinetic nystagmus after posterior suprasylvian lesions in the ferret (Mustela putorius furo). Exp. Brain Res. *182*, 509–523.
13. Hubel, D.H., and Wiesel, T.N. (1969). Visual area of the lateral suprasylvian gyrus (Clare-Bishop area) of the cat. J. Physiol. *202*, 251–260.
14. Philipp, R., Distler, C., and Hoffmann, K.P. (2006). A motion-sensitive area in ferret extrastriate visual cortex: an analysis in pigmented and albino animals. Cereb. Cortex *16*, 779–790.
15. Dreher, B., Wang, C., Turlejski, K.J., Djavadian, R.L., and Burke, W. (1996). Areas PMLS and 21a of cat visual cortex: two functionally distinct areas. Cereb. Cortex *6*, 585–599.
16. Toyama, K., Mizobe, K., Akase, E., and Kaihara, T. (1994). Neuronal responsiveness in areas 19 and 21a, and the posteromedial lateral suprasylvian cortex of the cat. Exp. Brain Res. *99*, 289–301.
17. Dreher, B. (1986). Thalamocortical and corticocortical interconnections in the cat visual system: Relation to the mechanisms of information processing. In Visual Neuroscience, J.D. Pettigrew, K.J. Sanderson, and W.R. Levick, eds. (Cambridge: Cambridge University Press), pp. 290–314.
18. Innocenti, G.M., Manger, P.R., Masiello, I., Colin, I., and Tettoni, L. (2002). Architecture and callosal connections of visual areas 17, 18, 19 and 21 in the ferret (Mustela putorius). Cereb. Cortex *12*, 411–422.
19. Manger, P.R., Kiper, D., Masiello, I., Murillo, L., Tettoni, L., Hunyadi, Z., and Innocenti, G.M. (2002). The representation of the visual field in three extrastriate areas of the ferret (Mustela putorius) and the relationship of retinotopy and field boundaries to callosal connectivity. Cereb. Cortex *12*, 423–437.
20. Morley, J.W., and Vickery, R.M. (1997). Spatial and temporal frequency selectivity of cells in area 21a of the cat. J. Physiol. *501*, 405–413.
21. Wimborne, B.M., and Henry, G.H. (1992). Response characteristics of the cells of cortical area 21a of the cat with special reference to orientation specificity. J. Physiol. *449*, 457–478.
22. Symonds, L.L., and Rosenquist, A.C. (1984). Corticocortical connections among visual areas in the cat. J. Comp. Neurol. *229*, 1–38.
23. Symonds, L.L., and Rosenquist, A.C. (1984). Laminar origins of visual corticocortical connections in the cat. J. Comp. Neurol. *229*, 39–47.
24. White, L.E., Bosking, W.H., Williams, S.M., and Fitzpatrick, D. (1999). Maps of central visual space in ferret V1 and V2 lack matching inputs from the two eyes. J. Neurosci. *19*, 7089–7099.
25. Yu, H., Farley, B.J., Jin, D.Z., and Sur, M. (2005). The coordinated mapping of visual space and response features in visual cortex. Neuron *47*, 267–280.
26. Bullier, J., Kennedy, H., and Salinger, W. (1984). Branching and laminar origin of projections between visual cortical areas in the cat. J. Comp. Neurol. *228*, 329–341.
27. Movshon, J.A., and Newsome, W.T. (1996). Visual response properties of striate cortical neurons projecting to area MT in macaque monkeys. J. Neurosci. *16*, 7733–7741.
28. DeAngelis, G.C., Freeman, R.D., and Ohzawa, I. (1994). Length and width tuning of neurons in the cat's primary visual cortex. J. Neurophysiol. *71*, 347–374.
29. Sceniak, M.P., Ringach, D.L., Hawken, M.J., and Shapley, R. (1999). Contrast's effect on spatial summation by macaque V1 neurons. Nat. Neurosci. *2*, 733–739.
30. Shapley, R., and Lennie, P. (1985). Spatial frequency analysis in the visual system. Annu. Rev. Neurosci. *8*, 547–583.
31. Douglas, R.J., and Martin, K.A. (1991). A functional microcircuit for cat visual cortex. J. Physiol. *440*, 735–769.
32. Livingstone, M.S., and Hubel, D.H. (1987). Psychophysical evidence for separate channels for the perception of form, color, movement, and depth. J. Neurosci. *7*, 3416–3468.
33. Maunsell, J.H. (1987). Physiological evidence for two visual subsystems. In Matters of Intelligence, L. Vaina, ed. (Dordrecht, Holland: Reidel), pp. 59–87.
34. Casagrande, V.A., and Royal, D. (2003). Parallel visual pathways in a dynamic system. In Primate Vision, J.H. Kaas and C.E. Collins, eds. (Boca Raton, FL: CRC Press), pp. 1–28.
35. Merigan, W.H., and Maunsell, J.H.R. (1993). How parallel are the primate visual pathways? Annu. Rev. Neurosci. *16*, 369–402.
36. Sincich, L.C., and Horton, J.C. (2005). The circuitry of V1 and V2: integration of color, form, and motion. Annu. Rev. Neurosci. *28*, 303–326.
37. Cleland, B.G., Dubin, M.W., and Levick, W.R. (1971). Sustained and transient neurones in the cat's retina and lateral geniculate nucleus. J. Physiol. *217*, 473–496.
38. Enroth-Cugell, C., and Robson, J.G. (1966). The contrast sensitivity of retinal ganglion cells of the cat. J. Physiol. *187*, 517–552.
39. Mazzoni, P., Andersen, R.A., and Jordan, M.I. (1991). A more biologically plausible learning rule than backpropagation applied to a network model of cortical area 7a. Cereb. Cortex *1*, 293–307.
40. Zipser, D., and Andersen, R.A. (1988). A back-propagation programmed network that simulates response properties of a subset of posterior parietal neurons. Nature *331*, 679–684.
41. Jarosiewicz, B., Chase, S.M., Fraser, G.W., Velliste, M., Kass, R.E., and Schwartz, A.B. (2008). Functional network reorganization during learning in a brain-computer interface paradigm. Proc. Natl. Acad. Sci. USA *105*, 19486–19491.

42. Soodak, R.E., Shapley, R.M., and Kaplan, E. (1987). Linear mechanism of orientation tuning in the retina and lateral geniculate nucleus of the cat. J. Neurophysiol. *58*, 267–275.
43. Vidyasagar, T.R., and Urbas, J.V. (1982). Orientation sensitivity of cat LGN neurones with and without inputs from visual cortical areas 17 and 18. Exp. Brain Res. *46*, 157–169.
44. Pack, C.C., and Born, R.T. (2001). Temporal dynamics of a neural solution to the aperture problem in visual area MT of macaque brain. Nature *409*, 1040–1042.
45. Movshon, J.A., Adelson, E.H., Gizzi, M.S., and Newsome, W.T. (1985). The analysis of moving visual patterns. In Experimental Brain Research Supplementum II: Pattern Recognition Mechanisms, C. Chagas, R. Gattas, and C.G. Gross, eds. (New York: Springer), pp. 117–151.
46. Beck, C., and Neumann, H. (2009). Area MT pattern motion selectivity by integrating 1D and 2D motion features from V1—a neural model. Front. Syst. Neurosci. conference abstract, Computational and Systems Neuroscience 2009. 10.3389/conf.neuro.06.2009.03.163.
47. Grossberg, S., and Mingolla, E. (1993). Neural dynamics of motion perception: direction fields, apertures, and resonant grouping. Percept. Psychophys. *53*, 243–278.
48. Schummers, J., Yu, H., and Sur, M. (2008). Tuned responses of astrocytes and their influence on hemodynamic signals in the visual cortex. Science *320*, 1638–1643.
49. Stosiek, C., Garaschuk, O., Holthoff, K., and Konnerth, A. (2003). In vivo two-photon calcium imaging of neuronal networks. Proc. Natl. Acad. Sci. USA *100*, 7319–7324.
50. Malik, W.Q., Schummers, J., Sur, M., and Brown, E.N. (2011). Denoising two-photon calcium imaging data. PLoS ONE *6*, e20490.
51. Manger, P.R., Engler, G., Moll, C.K., and Engel, A.K. (2005). The anterior ectosylvian visual area of the ferret: a homologue for an enigmatic visual cortical area of the cat? Eur. J. Neurosci. *22*, 706–714.

Current Biology, Volume *22*

Supplemental Information

Functional Biases in Visual Cortex Neurons with Identified Projections to Higher Cortical Targets

Beata Jarosiewicz, James Schummers, Wasim Q. Malik, Emery N. Brown, and Mriganka Sur

Supplemental Inventory

Figure S1. Related to Figure 1, showing detailed histology of the tracer injection sites and methods for obtaining tuning curves from the raw imaging data.

Figure S2. Related to Figure 2, separating the findings shown in Figure 2 by imaging region (area 17 vs. area 18), which shows that the differences in direction selectivity that we observe between projection cell groups cannot be accounted for by functional differences between the regions in which they were imaged. It also shows spatially-organized maps of direction selectivity for all cells from all imaging windows from all animals, which provides evidence for a possible relationship between anatomical and functional clustering of direction selectivity.

Figure S3. Related to Figure 3, separating the findings shown in Figure 3 by imaging region (area 17 vs. area 18). Also shows examples of raw and fitted length tuning curves for both projection cell types.

Figure S4. Related to Figure 4 in the same way as Figure S3 relates to Figure 3.

Figure S5. Related to Figure 5 in the same way as Figure S3 relates to Figure 3.

Figure S6. Related to Figure 6, showing the functional maps for all episodic features for all imaging sites.

Table S1. Shows detailed information about the animals used, including their ages, the delay between the tracer injection and imaging, which tracer was used in which downstream target, and the location of the imaging site.

Supplemental Experimental Procedures. Provides details on the methods.

Supplemental References

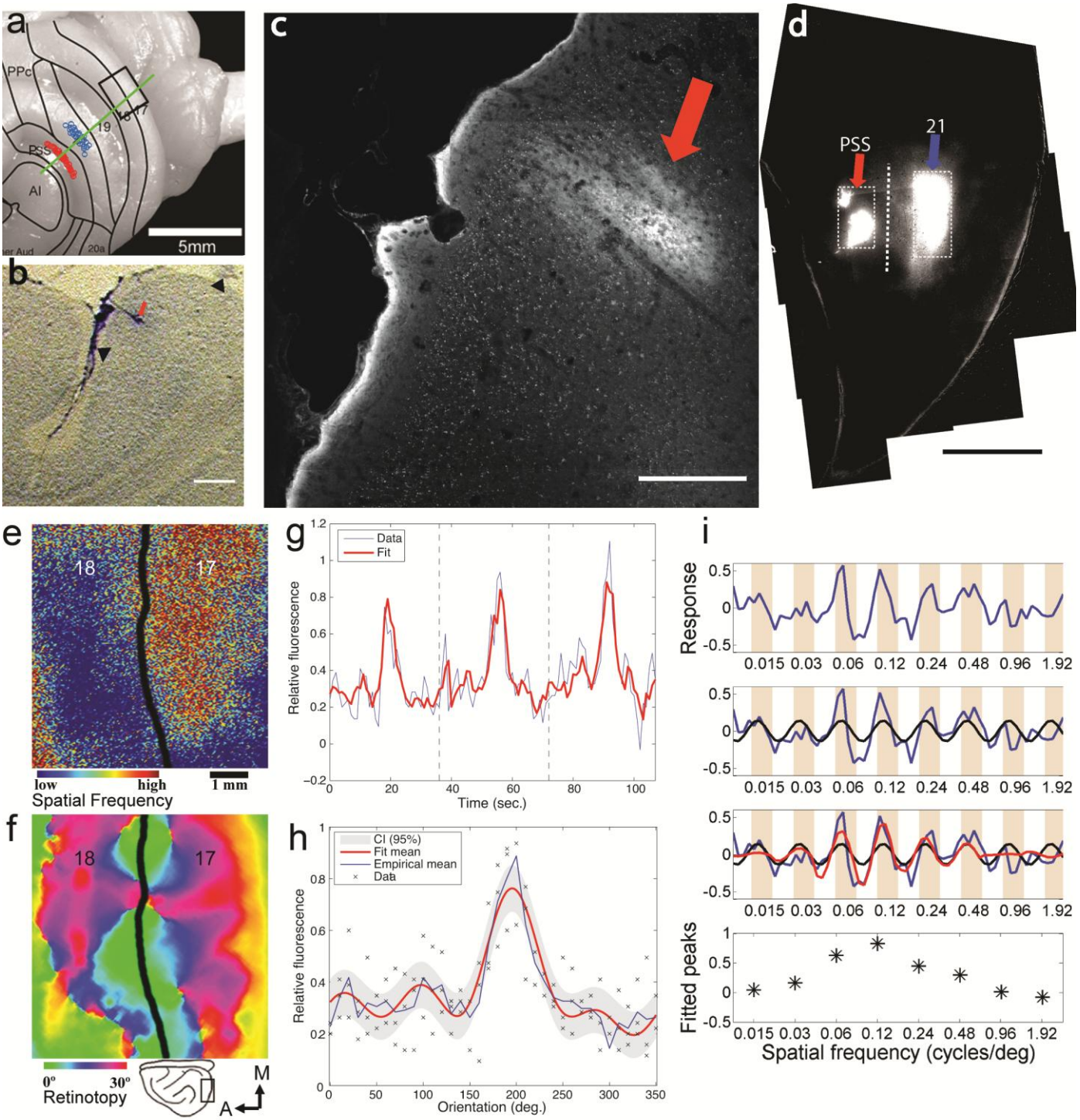

Figure S1. Detailed methods (related to Figure 1). (a-d) Histology. (a) Approximate sites of tracer injections across all animals are marked with *red* (PSS) and *blue* (area 21) *circles* overlaid on a photograph of the ferret brain (modified with permission from [1]). The *black rectangle* denotes the location of the imaging window, and the *dark green line* denotes both the plane of section of the images in (b) and (c) and the location of the -5 deg elevation line of visual field maps in areas 17, 18, 19, 21 and PSS [2, 3]. The *light green lines* schematically depict the locations of receptive fields between 0 deg and -15 deg elevation. Injections made at these locations in PSS and area 21 led to intermixed retrogradely labeled neurons in areas 17 and 18 within the imaging window. Scale bar: 5 mm. (b) A Nissl-stained parasagittal section showing an injection site (CTB-594) in PSS, located on the posterior bank of the suprasylvian sulcus and demarcated by black arrowheads. Scale bar: 600 um. (c) A fluorescence image of a section adjacent to the one shown in (b). The injection is confined to the gray matter, and no damage to the surrounding tissue is apparent. Scale bar: 300 um**.** (d) A tangential section from a different ferret showing two sets of injections sites. In each of areas PSS and 21 (separated by the dotted line), 3 closely spaced injections were made (see *Supplemental Experimental Procedures*). Each box shows these injections, one set in PSS (CTB-594) and another set in 21 (CTB-555). Scale bar: 2 mm. (e-f) Functional differences

between areas 17 and 18 and demarcation of the border between them using intrinsic signal optical imaging [4]. Region corresponds to box in (a). (e) Spatial frequency map created using low (0.08 cycle/degree) vs high (0.325 cycle/degree) spatial frequency gratings spanning the entire visual field (4 orientations, temporal frequency = 1Hz). Area 17 shows preference for higher spatial frequencies compared to area 18. Scale bar: 1 mm. (f) Azimuth axis of retinotopic maps in the same region in the same animal, derived from responses to a flashing bar moving from the center to the periphery continuously. Each cycle of the moving bar covered 30 degrees of visual field. The border between areas 17 and 18 was demarcated based on the spatial frequency responses and the reversal of the retinotopic map, as described previously [5]. We determined whether each imaging site in our experiment was located in area 17 or area 18 based on that site's overall spatial frequency preference, retinotopy, and distance from the posterior bend of cortex. (g-h) Obtaining tuning curves for periodic stimuli. For each cell, the fluorescence time series from each trial was filtered, baseline corrected, and scaled so that its amplitude ranged from 0 to 1. (g) The resulting signal (*blue trace*) was fitted (*red trace*) using a signal-plus-colored-noise model [6]: the signal component consisted of a multiple harmonic structure estimated using a least squares procedure, while the colored noise was modeled as an autoregressive process estimated using the Burg algorithm. (h) The signal component from the model provided a smoothed and denoised tuning curve (*red trace*) which was comparable in its overall trends to the empirical mean response (*blue trace*) of the raw responses at each stimulus value (*black crosses*). The *gray cloud* shows the 95% confidence interval of the estimated tuning curve. (i) Obtaining tuning curves for episodic stimuli. Steps are shown for one trial from one cell's responses to a grating stimulus whose spatial frequency is varied across each 'stimulus on' period (denoted in *beige*). For each cell, the fluorescence time series from each trial was filtered and baseline-corrected. The resulting signal (*blue trace*) was fitted to a 'carrier' sinusoid (*black trace*) whose frequency was constrained to match that of the stimulus on/off cycle and whose amplitude and phase were fitted to that trial's data using least-squares regression. Then a separate least-squares regression was done on each cycle of the carrier to obtain the amplitude of the carrier that best fit the data in that cycle (*red trace*). One set of response amplitudes (*black asterisks*) was thus obtained for each trial. These response amplitudes were then aligned across trials and a tuning curve was fit to the resulting data points, as described in the main text.

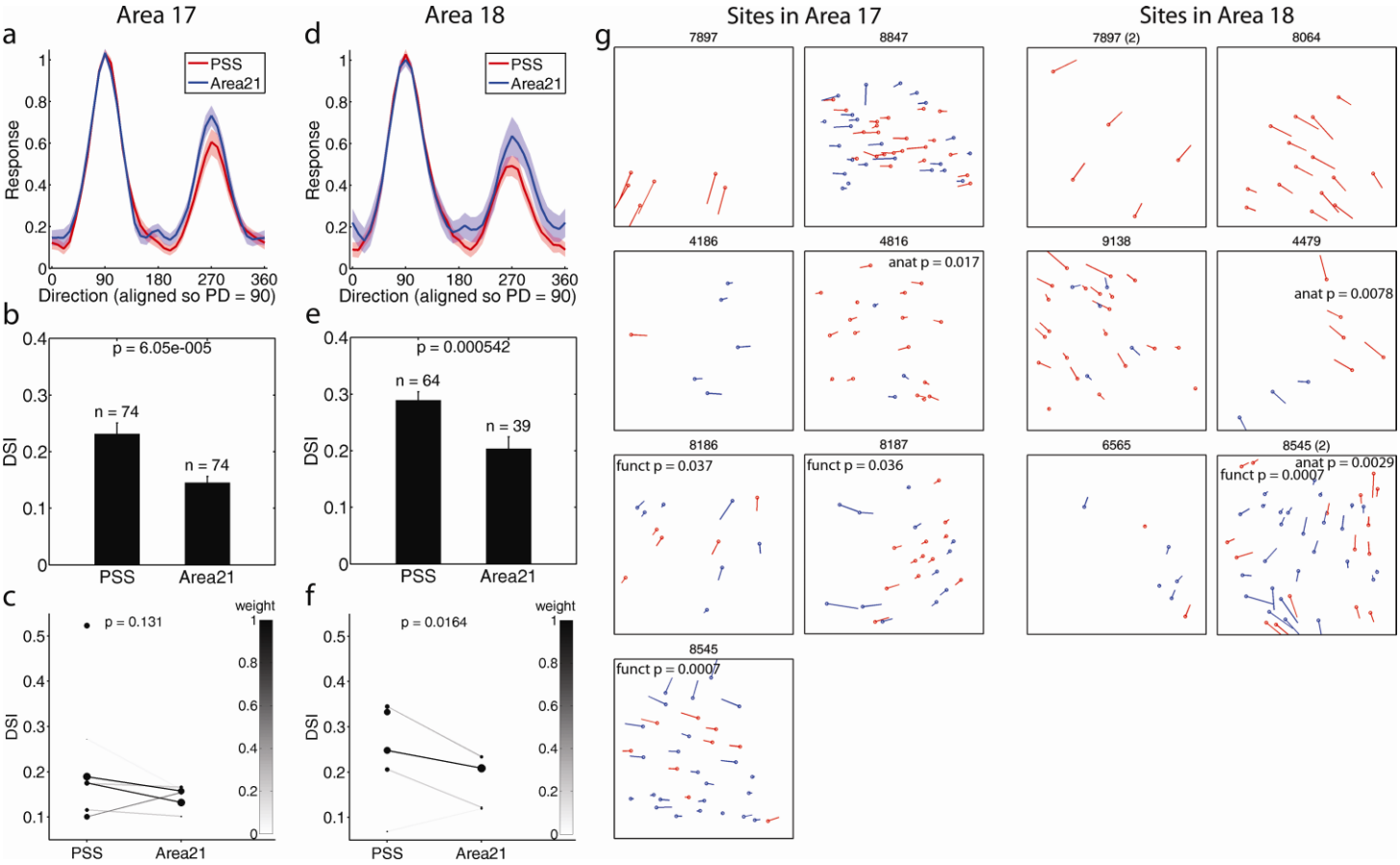

Figure S2. Direction selectivity results, segregated by location of imaging site (related to Figure 2). (a-c) Results for all imaging sites that were located within area 17. See Figure 2 of main text for details of analyses. (d-f) Results for all imaging sites that were located within area 18. (a,d) Weighted mean of raw tuning curves. (b,e) Weighted mean Direction Selectivity Index (DSI), with p-value from weighted t-test shown. (c,f) Within-site comparison of DSI. (g) A direction selectivity map was created for each imaging site (~250 x 250 um) by marking the center of each cell's location in the imaging site with a circle (*red* for cells projecting to PSS, and *blue* for cells projecting to area 21). Each cell's preferred motion direction is represented by a line extending from the circle, and its DSI is represented by the length of the line (longer lines represent stronger direction selectivity). Imaging sites in area 17 are shown on the *left* and those in area 18 are shown on the *right* (see also **Table S1**). Some imaging sites show significant functional ("funct") and/or anatomical ("anat") clustering (see *Supplemental Experimental Methods* and **Figure 6** in main text, and **Figure S6**); those panels are annotated with the corresponding p-values. Though there were no imaging sites with statistically significant correspondence between functional and anatomical clustering (see Figure 6 in main text), evidence for a possible larger-scale clustering correspondence comes from a comparison of the results across imaging sites: the PSS-projecting cells in the 3 imaging sites in which *only* PSS had been injected (7897, 7897(2), and 8064) had very high DSI's (see also Figure 2d), which is consistent with the possibility that regions in areas 17 and 18 that have high direction selectivity might correspond to regions with a high density of projections to the dorsal stream. Data from larger imaging sites would be required to fully test this possibility.

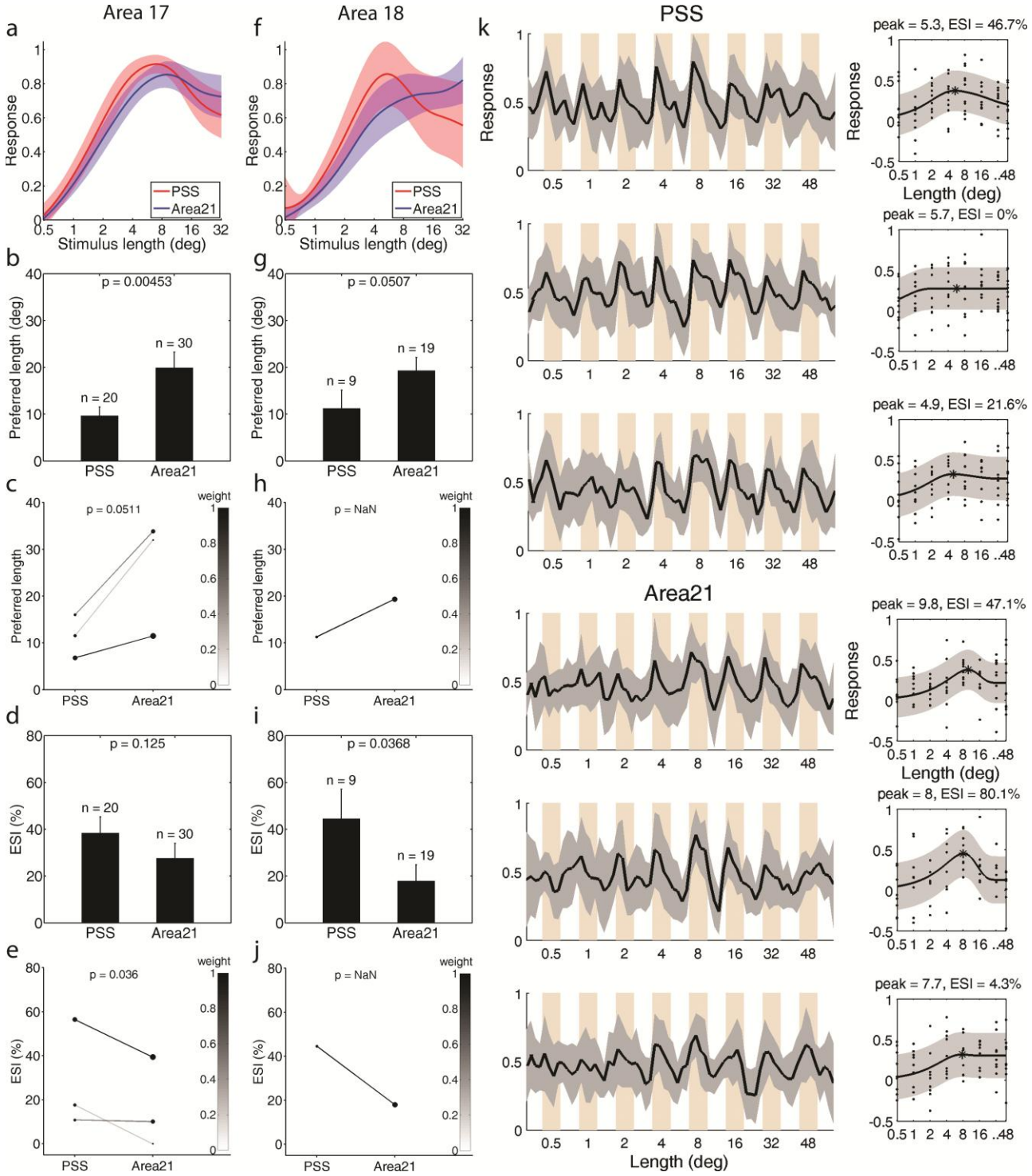

Figure S3. Length tuning results, segregated by location of imaging site (related to Figure 3). (a-e) Results for all imaging sites that were within area 17. (f-j) Results for all imaging sites that were within area 18. (a,f) Weighted mean of all tuning curves, fitted to the integral of a difference of Gaussians. (b,g) Weighted mean preferred length, with p-value from weighted T-test shown. (c,h) Within-site comparison of preferred length. (d,i) Weighted mean end-suppression index (ESI), with p-value from weighted t-test shown. (e,j) Within-site comparison of ESI. (k) Example length tuning curves of 3 PSS-projecting cells and 3 area 21-projecting cells. Each panel on the left shows the average baseline-corrected, scaled fluorescence time series across all trials (*black line*) and the standard error (*gray cloud*); the *beige shaded bars* are the 'stimulus on' periods. Each panel on the right shows the set of response amplitudes from all trials (*black dots*; see **Figure S1g**) and the fit of these data to the integral of a difference-of-Gaussians model (*solid black line*). Each example cell's peak (preferred) length and end-suppression index (ESI) is indicated above its fitted curve, and the peak length is marked with a '*' on the fitted curve.

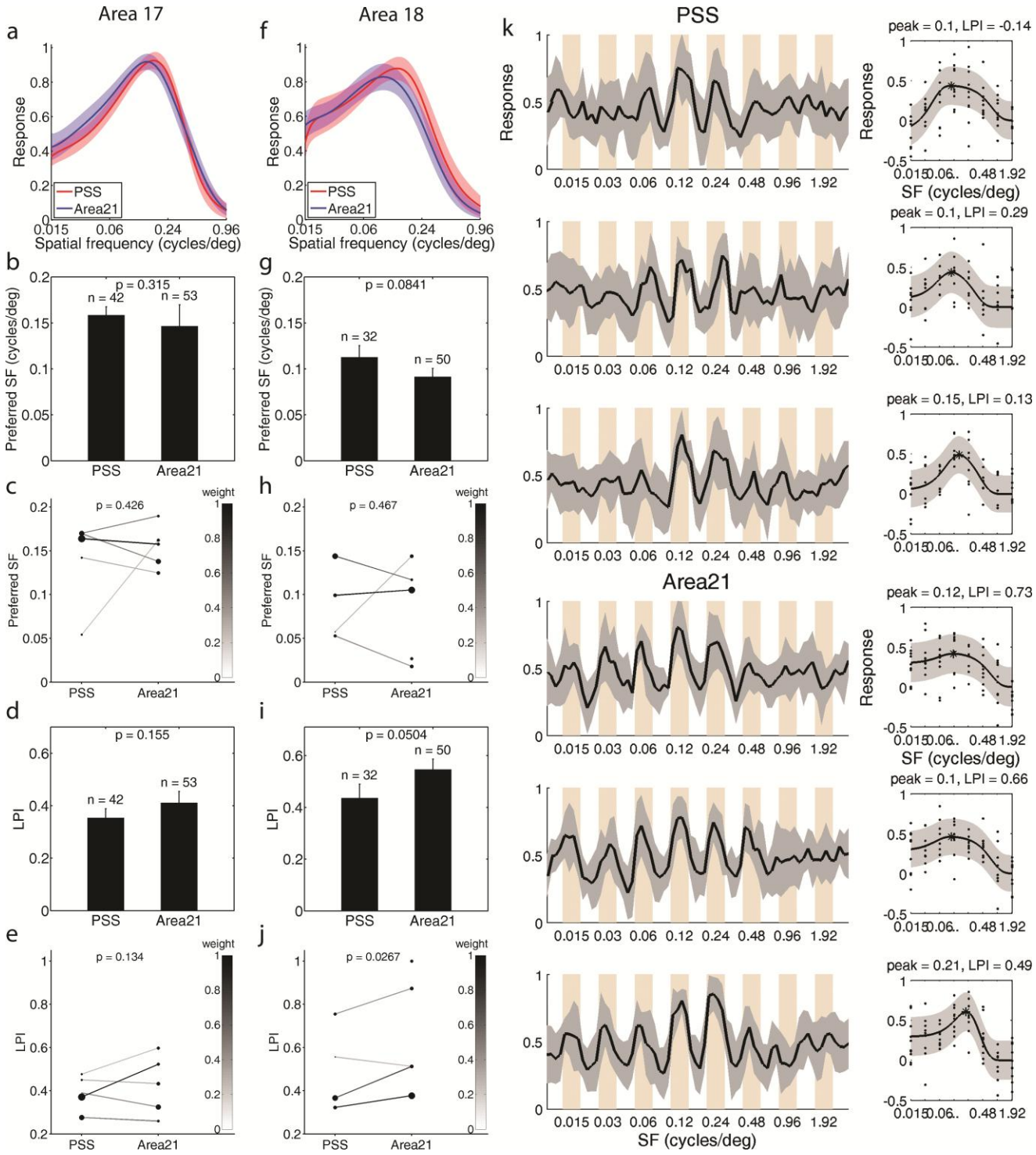

Figure S4. Spatial frequency tuning results, segregated by location of imaging site (related to Figure 4). (a-e) Results for all imaging sites that were within area 17. (f-j) Results for all imaging sites that were within area 18. (a,f) Weighted mean of all tuning curves, fitted to a difference of Gaussians. (b,g) Weighted mean preferred spatial frequency (SF), with p-value from weighted t-test shown. (c,h) Within-site comparison of preferred SF. (d,i) Weighted mean end-suppression index (ESI), with p-value from weighted t-test shown. (e,j) Within-site comparison of ESI. (k) SF tuning curves from 3 PSS-projecting and 3 Area 21-projecting cells. SF curves were fit using a difference-of-Gaussians model (*black line*; see *Supplemental Experimental Procedures* and **Figure S1g**). The peak SF and low-pass index (LPI, defined as the difference in the fitted response to the low minus the high SF, normalized by the height of the curve) are indicated above the fitted curve plots.

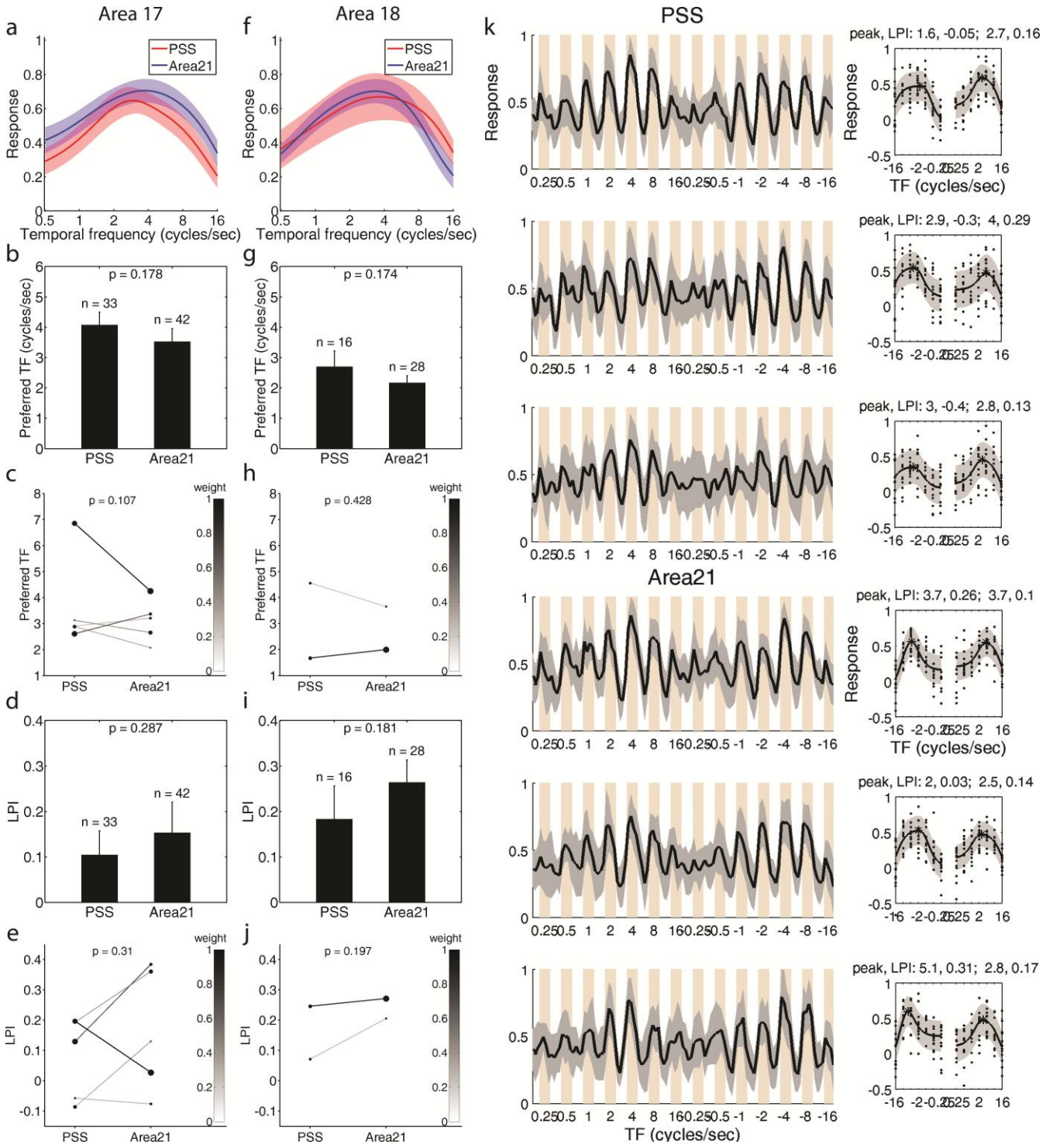

Figure S5. Temporal frequency tuning results, segregated by location of imaging site (related to Figure 5). (a-e) Results for all imaging sites that were within area 17. (f-j) Results for all imaging sites that were within area 18. (a,f) Weighted mean of all tuning curves, fitted to a difference of Gaussians. (b,g) Weighted mean preferred temporal frequency (TF), with p-value from weighted t-test shown. (c,h) Within-site comparison of preferred TF. (d,i) Weighted mean low-pass index (LPI), with p-value from weighted t-test shown. (e,j) Within-site comparison of LPI. (k) TF tuning curves from 3 PSS-projecting and 3 Area 21-projecting cells. TF curves were fit using a difference-of-Gaussians model (*black line*; see *Supplemental Experimental Procedures* and **Figure S1g**). The peak TF and low-pass index (LPI, defined as the difference in the fitted response to the low minus the high TF, normalized by the height of the curve) are indicated above the fitted curve plots. Because TF responses are known to differ in a cell's preferred drift direction than its non-preferred direction, and not all cells in a given imaging window had the same preferred direction, we presented the TF stimulus in both drift directions separately. Only the tuning curve in the preferred direction was used for subsequent analysis.

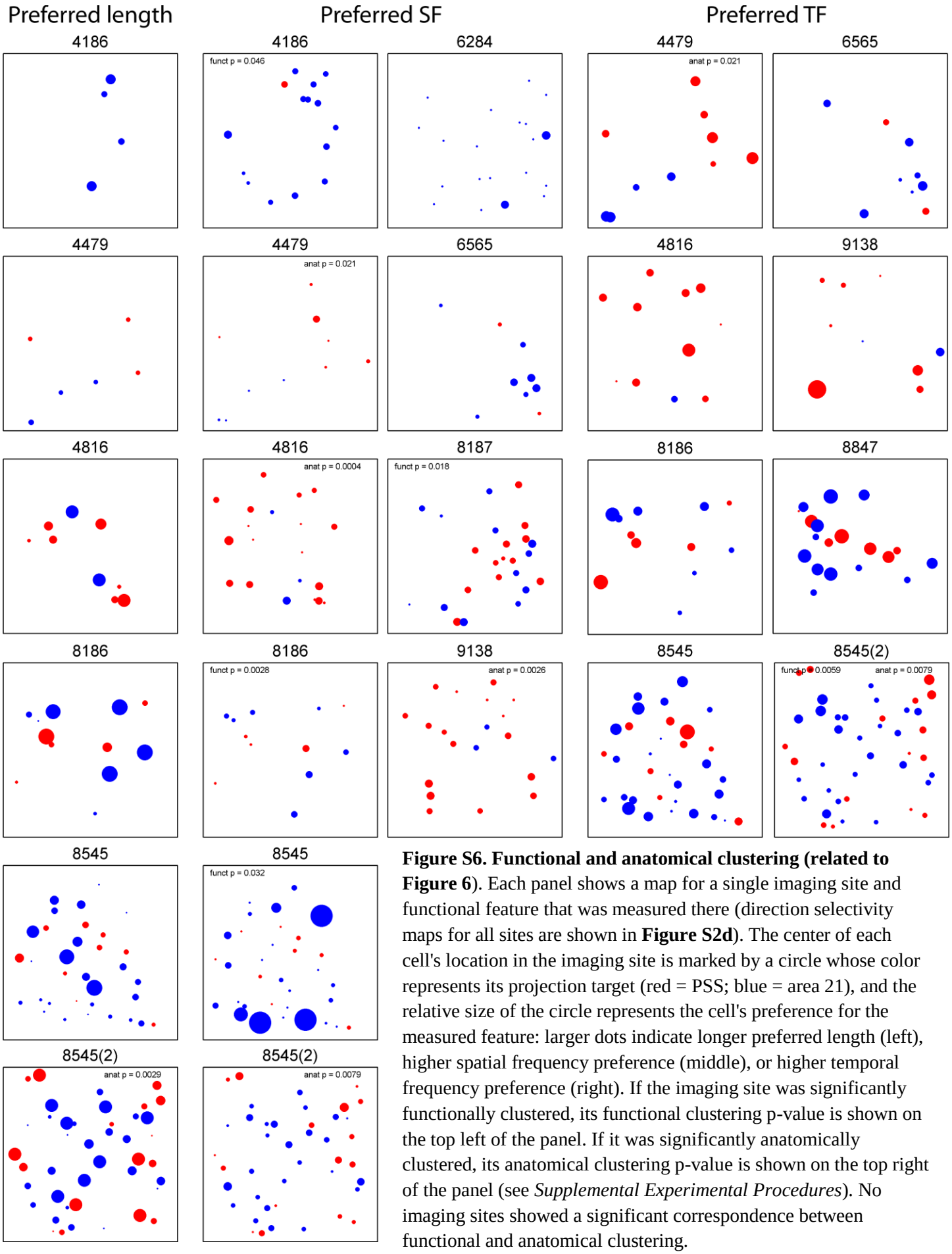

Figure S6. Functional and anatomical clustering (related to Figure 6). Each panel shows a map for a single imaging site and functional feature that was measured there (direction selectivity maps for all sites are shown in **Figure S2d**). The center of each cell's location in the imaging site is marked by a circle whose color represents its projection target (red = PSS; blue = area 21), and the relative size of the circle represents the cell's preference for the measured feature: larger dots indicate longer preferred length (left), higher spatial frequency preference (middle), or higher temporal frequency preference (right). If the imaging site was significantly functionally clustered, its functional clustering p-value is shown on the top left of the panel. If it was significantly anatomically clustered, its anatomical clustering p-value is shown on the top right of the panel (see *Supplemental Experimental Procedures*). No imaging sites showed a significant correspondence between functional and anatomical clustering.

animal #	age	delay	CTB-555	CTB-594	imaging site
7897	50	6		PSS*	Area 17
7897 (2)					Area 18
8064	44	7		PSS*	Area 18
8847	48	6	Area 21	PSS	Area 17
9138	68	7	PSS	Area 21	Area 18
4479	52	5	PSS	Area 21	Area 18
4186	78	12	PSS	Area 21	Area 17
4816	43	7	PSS	Area 21	Area 17
6284	51	7	Area 21	PSS	Area 18
6565	50	5	Area 21	PSS	Area 18
8186	43	6	PSS	Area 21	Area 17
8187	45	7	PSS	Area 21	Area 17
8545	41	6	Area 21	PSS	Area 17
8545 (2)					Area 18

Table 1. Animals Used in the Experiments

Animals are listed in the order in which they were used; when multiple sites were imaged in a single animal, there is a (2) indicating the second imaging site. 'Age' is the animal's age at the tracer injection surgery, and 'delay' is the delay from the tracer injection to imaging, in days. The CTB columns indicate in which brain area each tracer was injected. 'Imaging site' is the cortical area in which the imaging region was judged to be at the time of imaging (see text and **Figure S1**). *In these animals, only PSS was injected.

Supplemental Experimental Procedures

Animals and Tracer Injection Surgery

Experiments were performed on 12 male ferrets 41-78 days old at the start of the experiment. All experimental procedures were approved by the MIT Institutional Animal Care and Use Committee, and adhered to NIH guidelines. Animals were premedicated with atropine (0.04 mg/kg IM). Anesthesia was induced with ketamine (25 mg/kg IM) and xylazine (2 mg/kg IM) and maintained using isoflurane or sevoflurane (1.5-2.0%) in O_2. Skin and muscle were retracted over the posterior ~1.5 cm of the right hemisphere, and the posterior ~8 mm of skull was thinned using a stainless steel drill bit, allowing the suprasylvian sulcus (SS) and lateral sulcus (LS) to be visually identified. A small (~4x4 mm) craniotomy was made between the posterior bend of the SS and the lateral end of the LS, exposing PSS and area 21 [3, 7].

The dura was carefully retracted, and the tip of a glass micropipette loaded with tracer was lowered into the cortex using a stereotaxic micromanipulator. Three pressure injections of one tracer (1% of either CTB-555 or CTB-594 in sterile phosphate-buffered saline) were made along the mediolateral extent of PSS, which was anatomically identified as the strip of cortex on the posterior bank of SS (see **Figure S1**), and in 10 of the 12 animals, three injections of the other tracer were made along the mediolateral extent of area 21, which was anatomically identified as 2/3 of the way from SS to the lateral end of LS, ~2 mm caudal to the PSS injections. One uL of tracer was injected at each site, 0.5 uL at 0.7 mm below the pial surface, and 0.5 uL at 1.2 mm below the pial surface, at a rate of 0.1 uL/minute. Injection sites were carefully placed at locations identified anatomically and in some cases histologically as areas PSS and 21, and were confined to the grey matter of the cortex. Thus it is unlikely that our data were contaminated by fibers of passage.

The retracted dura was then folded back over the exposed cortex, the bone flap was replaced, and the craniotomy site was covered with Kwik-Sil silicone elastomer (World Precision Instruments, Sarasota, FL). The skin was sutured closed and the animal was allowed to recover in its cage. Buprenex analgesic (0.1 mg/kg SC) was administered just before anesthetic gases were discontinued and additionally every 12 hours for 3 days. Baytril antibiotic (5 mg/kg SC) was given prophylactically every 24 hours for 7 days or until the animal was imaged.

The cortical area in which each tracer was injected was counterbalanced across animals (see **Table S1**). Injections were targeted to cortical locations within PSS and area 21 representing similar, central locations of the visual field. The optimal injection sites had been identified previously in a pilot study by injecting the central visual field representation [3] of areas 17 and 18 with CTB-594 and locating the sites with densest anterograde labeling in PSS and area 21.

Two-Photon Imaging

Approximately 7 days following tracer injection surgery (range: 5 – 12 days; see **Table S1**), retrogradely labeled cells in areas 17 and/or 18 were characterized using 2-photon calcium imaging [8]. To prepare the animal for imaging, anesthesia was induced using ketamine (25 mg/kg IM) and xylazine (2 mg/kg IM) and maintained using isoflurane (1.5 - 2% in a 70:30 mixture of $N_20/0_2$). Throughout animal preparation and imaging, heart rate, temperature, and expired O_2 were monitored continuously; blood oxygen was maintained by controlling the volume of an artificial respirator and body temperature was maintained at 37.5 ºC using a heating blanket. Skin and muscle were retracted and a small metal headplate was attached to the skull with dental acrylic, which was then screwed to a raised platform on the movable stage of the 2-photon microscope. A craniotomy (~2 x 5 mm) was performed at the posterior end of cortex to expose the portion of area 17 and 18 that corresponded retinotopically to the previously injected areas of PSS and area 21. Dura was removed, and the exposed craniotomy was filled with 2% agarose in saline and sealed with a glass coverslip, leaving a ~1 mm gap between the coverslip and the lateral edge of the craniotomy through which the pipette tip containing OGB would later be inserted. A drop of 2.5% phenylephrine hydrochloride ophthalmic solution (Bausch & Lomb, Tampa, FL) and a drop of 1% atropine sulfate ophthalmic solution (Bausch & Lomb, Tampa, FL) were placed on each eye to retract the nictitating membrane and dilate the pupils, respectively; then the eyes were protected with either custom made contact lenses or a film of silicone oil (200 fluid, viscosity 50 cSt, Sigma-Aldrich, St. Louis, MO). Isoflurane was reduced to ~1%, and to prevent eye movements, Vecuronium bromide paralytic was injected (2.5 mg/kg bolus at the start of imaging, and then 0.25 mg/kg/hr, IP).

Two-photon imaging was performed using a custom-made microscope [9, 8]. Once a region in the cranial window was found that contained tracer-filled cells of both projection cell types, two Z-stacks were taken from the cortical surface to 250-300 um below the cortical surface at ~5 um increments, each with excitation and filter settings optimized for one of the tracers (CTB-594: 810 nm excitation, 653/95 nm emission bandpass; CTB-555: 725 nm excitation, 575/30 nm emission bandpass). A glass micropipette was then loaded with ~2.5 uL of freshly prepared 1.0 mM OGB1-acetoxymethyl ester (Molecular Probes, Eugene, OR) and inserted under visual guidance using a micromanipulator (Soma Scientific, Pacific Palisades, CA) so that the tip was ~200 um below the cortical surface and centered at the chosen imaging site. A Picospritzer (General Valve) was used to inject enough OGB solution (~400 fL) to label a sphere of cells ~300-400 um in diameter (Stosiek et al., 2003) over ~1 minute. After the OGB was loaded into the cells (~45 min – 1 hour), another set of

Z-stacks was taken with an additional channel for imaging OGB (using a 540/40 emission filter). A 565 nm dichroic was used to further separate the OGB emission from the tracer emission.

An imaging depth was selected in the OGB-injected region that contained a large number of traced cells (usually 125-175 um below the pial surface, corresponding to layers 2/3), and 256x256 pixel (~250x250 um) images were captured from this plane at 1 Hz using FluoView (Olympus) software while visual stimuli (see below) were presented using the Psychophysics Toolbox [10] for Matlab (Mathworks, Natick, MA) on an LCD monitor placed ~10 cm in front of the animal. Images from two channels were collected simultaneously using an excitation wavelength of 810 nm, one channel for CTB-594 and one for OGB fluorescence. CTB-555 filled cells were identified *post-hoc* by aligning these functional data with the previously obtained Z-stacks.

Data Preprocessing

Where across-frame or across-trial image motion in the functional image stacks exceeded ~1 um in the imaging (x-y) plane, TurboReg [11] was used to align all frames and all trials using rigid-body image registration (imaging sites with larger motion than ~5 um in the imaging plane or with more than ~1 um motion in depth were discarded). All remaining processing, except as noted, was done using custom software written in Matlab.

High-frequency noise in the functional image stacks was reduced by convolution with a 3-dimensional (2 spatial and 1 temporal), 3-point Gaussian. To reduce any slow drift in the baseline signal over time in a given trial, the drift in the average time series (averaged over x-y) was estimated by convolving the average time series with a wide (36-point) Gaussian, and then the estimated drift at each time point was subtracted from all pixels in the corresponding time point of the functional image stack. This baseline correction also served to remove the DC offset of the signal, which was necessary for across-trial data analysis because absolute fluorescence values varied widely and arbitrarily across trials (e.g. with changes in laser power, the amount of ambient light reaching the preparation, the amount of OGB loaded into the cells, etc.). Regions of interest (ROIs) corresponding to tracer-labeled cells in the smoothed and drift-corrected fluorescence time series were then manually selected as described above. Each cell's time series from one trial was calculated by averaging the time series of each pixel in that cell's ROI during that trial. Tuning curves were obtained from these time series as described in the next two sections.

As expected from projections in cat visual cortex, double-labeled cells were rare [12]: in ferrets in which injections were small and well localized (9 of the 10 animals with injections in both PSS and area 21), no double-labeled cells were found, though injections were made in matched retinotopic locations in PSS and area 21 and retrogradely labeled cells were intermingled in area 17 or 18. In one animal that received more voluminous tracer injections, some double-labeled cells were observed. Because PSS and area 21 are anatomically adjacent (see **Figure 1** and **Figure S1**), we interpreted this double labeling as caused by overlap of the tracers at the injection sites. Thus, because their actual projection targets could not be ascertained, we did not include any double-labeled cells in the results reported here.

Direction and Orientation Selectivity

A "periodic" stimulus presentation paradigm was used for assessing direction and orientation selectivity: continuously drifting square or sinusoidal gratings whose orientation and drift direction (which was orthogonal to the orientation) changed by 10 degree increments every second were presented at 100% contrast. The spatial and temporal frequencies of the drifting gratings were set to values that elicited maximal responses from the imaged region, as judged by preliminary on-line analysis (typically 1.5 – 3 Hz TF and 0.12 Hz SF). Each trial consisted of three cycles around the circle, and each trial was repeated 3-10 times during the course of an experiment, or until reasonably clean direction tuning curves were discernable for multiple cells.

The drift-corrected fluorescence time series from each trial were scaled from 0 to 1 and concatenated to form a single periodic time series from which a tuning curve was obtained by fitting a signal-plus-colored-noise model [6] (**Figure S1 e-f**). Briefly, the signal component (the stimulus-evoked response) was fit using a harmonic regression, which can be written as

$$s_k = \mu + \sum_{h=1}^{H} \{a_h \cos(h\theta_k) + b_h \sin(h\theta_k)\} \qquad 1$$

where θ_k is the instantaneous orientation of the grating stimulus, μ is the intercept, a_h and b_h are the coefficients of the h^{th} harmonic, and H is the number of harmonics included in the model. From Fourier theory, the multiple harmonic model provides a flexible basis that, given the appropriate number of terms, can be used to approximate any periodic function. The noise component, on the other hand, is modeled as a p^{th} order autoregressive (AR) process, given by

$$v_k = \sum_{m=1}^{p} c_m v_{k-m} + \varepsilon_k \quad (2)$$

where c_m are the AR coefficients and $\varepsilon_k \sim \mathcal{N}(0, \sigma_\varepsilon^2)$ is the residual white noise with variance σ_ε^2.

The harmonic coefficients were estimated by a weighted least squares procedure, while the AR coefficients and noise variance were estimated using the Burg algorithm. The joint coefficient estimation was performed iteratively, exploiting the special structure of the AR process to derive an efficient and robust cyclic descent algorithm. Typically about 5 recursions were found to be sufficient for the iterative coefficient estimates to converge. The optimal model orders, *H* and *p*, were determined by the Akaike information criterion (AIC), and *H* = 4 and *p* = 5 were found to be most appropriate. The Ljung-Box test was used to verify that the residual, ε_k, was white and Gaussian, confirming that the variance in the fluorescence time series data was well explained by the two components, namely the stimulus-evoked activity (signal) and the stimulus-free activity (colored noise).

The direction selectivity index (DSI) was obtained from the fitted tuning curves using 2 common methods. The first was a vector average of the responses over the whole tuning curve, computed as:

$$DSI = \frac{\sqrt{\sum(R(\theta_k)\sin\theta_k)^2 + \sum(R(\theta_k)\cos\theta_k)^2}}{\sum R(\theta_k)} \quad (3)$$

where θ_k is the movement angle of the *k*th grating stimulus (ranging from 0 to 350 deg at 10 deg increments), and $R(\theta_k)$ is the response magnitude at the *k*th angle. Thus, DSI = 0 if the cell is not direction selective and 1 if it is maximally direction selective. The second method of computing direction selectivity (DSI_p) compared the heights of the peaks in the preferred and non-preferred direction: DSI_p = (P-N)/(P+N). The preferred direction (P) was defined as the peak of the tuning curve, and the non-preferred direction (N) was defined as the location of the next highest peak that was separated from the first one by at least 90 degrees. Thus, again, DSI_p = 0 if the cell is not direction selective and 1 if it is maximally direction selective.

Orientation selectivity was also calculated using two common methods. An Orientation Selectivity Index (OSI) was computed using a vector average analogous to the DSI vector average above, but using only the orientation tuning curve (i.e. the 180 deg of the direction tuning curve centered around the preferred direction). Each θ_k was first doubled to stretch the 180 deg over the circle, such that OSI = 0 when the tuning is flat across the 180 deg and OSI = 1 when it is maximally sharp:

$$OSI = \frac{\sqrt{\sum(R(\theta_k)\sin 2\theta_k)^2 + \sum(R(\theta_k)\cos 2\theta_k)^2}}{\sum R(\theta_k)} \quad (4)$$

The second method for measuring orientation selectivity was the half-width at half-height of the fitted curve (because the fitted curves were not constrained to be symmetrical, this was obtained by dividing the full width at half-height by 2.) When comparing these indices across cell groups, the signal-to-noise ratio (SNR) obtained from the harmonic model was used to weight each cell in the statistical analyses, thus giving more weight to cells that whose activity contained more information about that parameter (as described in *Statistical analysis* section, below).

Length, Spatial Frequency, And Temporal Frequency Tuning

An "episodic" stimulus presentation paradigm was used to assess length, spatial frequency, and temporal frequency tuning. In each trial, 4 baseline frames were captured with no stimulus on the screen, then the stimulus was 'on' for 4 frames, 'off' again for 4 frames, etc. Each time the stimulus came on, the parameter of a sinusoidal grating whose tuning function was being measured (length, SF, or TF) was varied along a $\log_2$ scale while the rest of the parameters were held constant at values that elicited maximal responses from the entire imaged plane, as judged by preliminary on-line analysis. Responses during the 'off' periods were used to estimate the baseline fluorescence. Each trial consisted of one pass through all values for the varied parameter, and trials was repeated 6-10 times during the course of an experiment, or until reasonably clean average responses were discernable for multiple cells. As with the stimulus used for assessing direction selectivity, the SF and TF stimuli were presented in a square aperture in a location on the monitor and with a stimulus size that elicited maximal responses from the imaging region. The length stimulus, however, was a rectangle whose width contained one cycle of a sinusoidal grating at optimal orientation and spatial frequency, and whose length was parametrically varied in the direction of the optimal orientation.

To obtain tuning curves for the episodic stimuli, each trial's fluorescence time series was filtered and baseline-corrected as described above. Because of the slow dynamics of the OGB signal relative to our data acquisition frame rate, the resulting signal could be modeled as an amplitude modulated signal whose carrier frequency matched that of the

stimulus 'on'/'off' cycle, and whose amplitude varied over time depending on the cell's relative preference for the stimulus shown during each 'on' period (**Figure S1g**). Thus a carrier sinusoid, $C(x) = \beta_1 \cos x + \beta_2 \sin x$, was first fit by least squares regression for each trial of each cell, where one cycle of x contains 2 baseline frames (with the stimulus off), 4 frames with the stimulus on, and then 2 more baseline frames. The optimal phase of the carrier could vary from cell to cell depending on its location along the scan path during imaging; it could also vary from trial to trial for a given cell because of slight variations in the timing of the onset of stimulus presentation relative to the onset of data acquisition in a given trial. The optimal phase estimate is obtained as a result of the estimation of parameters β_1 and β_2.

Trials in which the fitted carrier amplitude was less than 1/10 of the total range of the signal (i.e. trials that showed very little modulation with stimulus presentation) were excluded from further analysis. Also, unresponsive cells (i.e. ones that did not sufficiently modulate their activity with the stimulus on/off cycles) were excluded from further analysis. Modulation was quantified as the total carrier amplitude across all trials; we set the cutoff at 0.8 (i.e. cells were included if they had at least 8 minimally-responsive trials, or fewer trials with better responsiveness, which roughly corresponded to our subjective judgment of which cells were and were not responsive). This excluded approximately 15% of the cells in the episodic experiments, but the results were comparable with modulation cutoffs ranging from 0.5 to 1. For the remaining "responsive" cells and trials, the carrier amplitude was scaled to 1, and a separate least-squares regression was performed on each cycle of the carrier vs. the corresponding cycle of the fluorescence signal to determine which amplitude of the carrier in that cycle best fit the signal. Thus, an amplitude of 1 indicated a strong response in that cycle, 0 indicated no response, and a negative amplitude indicated a decrease in activity from baseline.

This process resulted in a set of best-fit response amplitudes for each stimulus parameter value, with one amplitude per parameter value per trial, to which tuning curves were fit as follows. For SF and TF tuning, the response amplitudes were fit to a difference-of-Gaussians (DoG) model [13], and for length tuning, the response amplitudes were fit to the integral of a DoG model [14], by weighted least-squares regression using Matlab's *nlinfit* (see **Figures S3-5**). The weight for each trial was the amplitude of the carrier sinusoid in that trial (thus giving more weight to trials in which the cell was more responsive). For length tuning, the integral of a DoG is the expected shape of the tuning curve if the cell's response to a given stimulus is proportional to the amount by which it stimulates the cell's on-center vs. its off-surround [14],

$$R_{length} = k_e \int_{y=-s/2}^{s/2} e^{-(\frac{2y}{a})^2} dy - k_i \int_{y=-s/2}^{s/2} e^{-(\frac{2y}{b})^2} dy \quad (5)$$

where k_e and a are free parameters determining the amplitude and width of the Gaussian on-center, respectively, and k_i and b are free parameters for the Gaussian off-surround (modified from [14], who also included a parameter for an offset between the center of the on and off regions, and a DC offset response, which we did not include because our response amplitudes were defined to have a minimum of 0). For SF tuning, the power spectrum of the assumed DoG-shaped receptive field, which is itself a DoG centered at zero [13],

$$R_{SF,TF} = k_e\, e^{-(\frac{2y}{a})^2} - k_i\, e^{-(\frac{2y}{b})^2} \quad (6)$$

is the expected shape of the tuning curve if the phase of the grating is centered on the receptive field such that the on-center and off-surround align with the oscillations of the grating at the optimal SF [13]. Our grating stimulus was a drifting one (drift was necessary to activate a large number of cells effectively), so the activity of simple cells would be expected to peak only when the grating's phase aligns with its receptive field [15], which might decrease their total responsiveness and increase their variability when measured at our sampling rate (1 Hz) using 2-photon calcium imaging. However, most of our cells were likely to be complex cells, which respond more continuously to drifting stimuli; though the reasoning behind using a DoG to model the SF responses of complex cells is not as straightforward as for simple cells, visual inspection of the tuning curve fits reveals that the model nevertheless worked well for our cells. For TF tuning, a standard model has not been developed yet, but we used the same model as we used for SF because, for drifting gratings, TF and SF are analogous in that they both denote the number of contrast inversions per unit time in a given patch of visual space (e.g. in a cell's receptive field). Again, we found by visual inspection that the DoG model fit our TF responses well.

Once a tuning curve was obtained for each cell, tuning preferences were compared between cell groups by obtaining the preferred SF, TF, or stimulus length for each cell, defined by the peak of its tuning curve. Because these tuning curves were often asymmetric, having fatter tails on one side or the other of the peak or monotonically increasing or decreasing, a 'low-pass index' (LPI = (L-H)/Amp, where L is the fitted response to the lowest and H to the highest stimulus value that was shown to all cells, and Amp is the amplitude of the peak response), was also calculated to characterize this asymmetry as another measure of stimulus preferences. To obtain a measure of tuning quality for each cell in the weighted statistical analyses (described in the next section), each cell's tuning curve was scaled from 0 to 1, and

the SE obtained from the tuning curve regression was scaled using the same scaling factor to obtain SE_{sc}. The weight of that cell in subsequent analyses was defined as $w_i = 1/SE_{sc}^2$. Thus, each cell was weighted by its effective signal-to-noise ratio, such that cells whose activity contained more information about a given parameter had higher weights than cells that contained less information about that parameter (see *Statistical analysis* below).

Statistical Analysis

The cells we imaged varied considerably in the signal-to-noise ratio of their tuning responses and tuning curves due to many uncontrolled factors (e.g., the degree to which that cell's activity is actually influenced by changes in the parameter under investigation, the amount of calcium dye that cell took up, the general condition of the animal and the cranial window when the cell was imaged, etc.). Instead of ignoring these important sources of variability, or simply discarding cells whose tuning quality for a given parameter did not exceed some arbitrary threshold, we used weighted statistics, which are more reliable than unweighted statistics for samples with unequal variance [16–18]. (For a textbook treatment of weighted statistics, see [18]; for a derivation, see [16]; and for a detailed description of weighted statistics applied in a similar context, see [17]). Briefly, the weighted mean $\overline{X}$ of the quantity X (where X could be DSI, OSI, LPI, etc.) was calculated using the standard formula

$$\overline{X} = \frac{\sum X_i w_i}{\sum w_i} \quad (7)$$

where X_i is the observation for cell i and w_i is its weight, defined as described in the preceding section. The variance of the weighted mean σ^2 for cell group g, corrected for dispersion, was calculated as

$${\sigma_g}^2 = \frac{1}{(n-1)} \times \frac{\sum_{i=1}^{n}(X_i - X)^2 w_i}{\sum_{i=1}^{n} w_i}, \quad (8)$$

where n is the number of cells in that cell group. The standard error of the weighted mean for cell group g is then

$$SE_g = \sqrt{{\sigma_g}^2} \quad (9)$$

To test for differences in the weighted means of the two cell populations, $\bar{X}_{PSS}$ vs. $\bar{X}_{Area21}$, a weighted t-statistic was calculated as

$$t = \frac{\bar{X}_{PSS} - \bar{X}_{Area21}}{\sqrt{{SE^2}_{PSS} + {SE^2}_{Area21}}} \quad (10)$$

where SE_g is the standard error of the weighted mean of cell group g. For a large number of units (as in our data), this t-statistic will have an approximately normal distribution, which we used to obtain the reported p-values.

The above t-tests treated all cells across all imaging sites as independent samples. To control for other factors that might affect neural responses, such as eccentricity of a given imaging site or the animal's depth of anesthesia, we also tested whether differences between cell groups exist *within* each imaging site. This analysis ensures that all of these uncontrolled factors are identical between cell groups, so that the only remaining factor that can account for tuning differences is the cell group's projection target. For each tuning parameter being compared, the weighted mean $X_{g,d}$ was obtained for each of the two cell groups g in each imaging site d that had at least 1 cell of each type, using equations *5-7*. Each imaging site's pair of means was then used as one sample in a paired t-test, weighting each imaging site by the total number of cells in that imaging site.

To test for anatomical clustering (i.e. to test whether cells with the same projection targets tended to be nearer to each other than cells with different projection targets), in each imaging site containing at least 2 cells of each projection target group, an anatomical clustering ratio (ACR) was computed from the distance of all nearest-neighbor cell pairs with the same vs. the opposite projection target. The same-group ACR was defined as the distance to the closest cell divided by the distance to the closest cell with the same projection target [19]; thus, a same-group ACR of 1 indicates that a given cell's nearest neighbor has the same projection target. To test for significance, a different-group ACR was also computed, defined as the distance to the closest cell divided by the distance to the closest cell with a *different* projection target (thus, a different-group ACR of 1 indicates that a given cell's nearest neighbor has a different projection target). Same-group ACR's were compared to different-group ACRs using a Sign test, which is a non-parametric test of the hypothesis that there is no difference in medians between the two groups that does not make assumptions about the shapes of their distributions.

To test for functional clustering in each imaging site (i.e. to test whether cells that are near each other tend to have similar functional properties), the absolute difference in the tuning for the measured parameter in that imaging site (e.g. DSI, TF preference, etc.) was computed for each nearest-neighbor cell pair. To test for significance, the probability of having observed the weighted mean nearest-neighbor functional difference for that imaging site by chance (i.e. the site's p-value) was obtained by comparing it to a bootstrapped null distribution of weighted means, which was obtained by randomly shuffling the functional preferences of those cells and finding their weighted means 10,000 times.

To test for a correspondence between anatomical and functional clustering, the functional difference was obtained for each nearest-neighbor pair as described above, but now each cell pair was also classified as anatomically same-group (if the two cells had the same projection target) or different-group (if the two cells had different projection targets). Imaging sites were only tested for functional-anatomical clustering correspondence if they were independently significant for both anatomical clustering and functional clustering for the parameter of interest. To test for significant correspondence between functional and anatomical clustering, a weighted t-test was used to compare the same-group to the different-group nearest-neighbor functional differences.

Supplemental References

1. Manger, P. R., Engler, G., Moll, C. K., and Engel, A. K. (2005). The anterior ectosylvian visual area of the ferret: a homologue for an enigmatic visual cortical area of the cat? Eur J Neurosci *22*, 706-714.
2. Cantone, G., Xiao, J., and Levitt, J. B. (2006). Retinotopic organization of ferret suprasylvian cortex. Vis Neurosci *23*, 61-77.
3. Manger, P. R., Kiper, D., Masiello, I., Murillo, L., Tettoni, L., Hunyadi, Z., and Innocenti, G. M. (2002). The representation of the visual field in three extrastriate areas of the ferret (Mustela putorius) and the relationship of retinotopy and field boundaries to callosal connectivity. Cereb Cortex *12*, 423-437.
4. Yu, H., Farley, B. J., Jin, D. Z., and Sur, M. (2005). The coordinated mapping of visual space and response features in visual cortex. Neuron *47*, 267-280.
5. White, L. E., Bosking, W. H., and Fitzpatrick, D. (2001). Consistent mapping of orientation preference across irregular functional domains in ferret visual cortex. Vis Neurosci *18*, 65-76.
6. Malik, W. Q., Schummers, J., Sur, M., and Brown, E. N. (2011). Denoising two-photon calcium imaging data. PloS One *6*, e20490.
7. Philipp, R., Distler, C., and Hoffmann, K. P. (2006). A motion-sensitive area in ferret extrastriate visual cortex: an analysis in pigmented and albino animals. Cereb Cortex *16*, 779-790.
8. Stosiek, C., Garaschuk, O., Holthoff, K., and Konnerth, A. (2003). In vivo two-photon calcium imaging of neuronal networks. Proc Natl Acad Sci U S A *100*, 7319-7324.
9. Schummers, J., Yu, H., and Sur, M. (2008). Tuned responses of astrocytes and their influence on hemodynamic signals in the visual cortex. Science *320*, 1638-1643.
10. Brainard, D. H. (1997). The Psychophysics Toolbox. Spat Vis *10*, 433-436.
11. Thevenaz, P., Ruttimann, U. E., and Unser, M. (1998). A pyramid approach to subpixel registration based on intensity. IEEE Trans Image Process *7*, 27-41.
12. Ferrer, J. M., Kato, N., and Price, D. J. (1992). Organization of association projections from area 17 to areas 18 and 19 and to suprasylvian areas in the cat's visual cortex. J Comp Neurol *316*, 261-278.
13. Shapley, R., and Lennie, P. (1985). Spatial frequency analysis in the visual system. Annu Rev Neurosci *8*, 547-583.
14. DeAngelis, G. C., Freeman, R. D., and Ohzawa, I. (1994). Length and width tuning of neurons in the cat's primary visual cortex. J Neurophysiol *71*, 347-374.
15. Skottun, B. C., De Valois, R. L., Grosof, D. H., Movshon, J. A., Albrecht, D. G., and Bonds, A. B. (1991). Classifying simple and complex cells on the basis of response modulation. Vision Res *31*, 1079-1086.
16. Goldberg, L. R., Kercheval, A. N., and Lee, K. (2005). t-Statistics for weighted means in credit risk modelling. Journal of Risk Finance *6*, 349-365.
17. Jarosiewicz, B., Chase, S. M., Fraser, G. W., Velliste, M., Kass, R. E., and Schwartz, A. B. (2008). Functional network reorganization during learning in a brain-computer interface paradigm. Proc Natl Acad Sci U S A *105*, 19486-19491.
18. Taylor, J. R. (1996). An Introduction to Error Analysis: The Study of Uncertainties in Physical Measurements (University Science Books).
19. Runyan, C. A., and Sur, M. Two distinct subtypes of PV+ inhibitory interneurons in mouse primary visual cortex. In Program No. 377.07. Neuroscience Meeting Planner. Washington, DC: Society for Neuroscience, 2011. Online.